

# Ab Initio Melting Properties of Water and Ice from Machine Learning Potentials

Yifan Li,<sup>1,\*</sup> Bingjia Yang,<sup>1</sup> Chunyi Zhang,<sup>2</sup> Axel Gomez,<sup>1</sup> Pinchen Xie,<sup>3</sup> Yixiao Chen,<sup>3</sup> Pablo M. Piaggi,<sup>4,5</sup> and Roberto Car<sup>1,3,6,7,†</sup>

<sup>1</sup>*Department of Chemistry, Princeton University, Princeton, NJ 08544, USA*

<sup>2</sup>*Eastern Institute of Technology, Ningbo, Zhejiang 315200, China*

<sup>3</sup>*Program in Applied and Computational Mathematics, Princeton University, Princeton, NJ 08544, USA*

<sup>4</sup>*CIC nanoGUNE BRTA, Tolosa Hiribidea 76, 20018 Donostia-San Sebastián, Spain*

<sup>5</sup>*Ikerbasque, Basque Foundation for Science, 48013 Bilbao, Spain*

<sup>6</sup>*Department of Physics, Princeton University, Princeton, NJ 08544, USA*

<sup>7</sup>*Princeton Institute for the Science and Technology of Materials, Princeton University, Princeton, NJ 08544, USA*

(Dated: January 1, 2026)

Liquid water exhibits several important anomalous properties in the vicinity of the melting temperature ( $T_m$ ) of ice Ih, including a higher density than ice and a density maximum at 4 °C. Experimentally, an isotope effect on  $T_m$  is observed: the melting temperature of H<sub>2</sub>O is approximately 4 K lower than that of D<sub>2</sub>O. This difference can only be explained by nuclear quantum effects (NQEs), which can be accurately captured using path integral molecular dynamics (PIMD). Here we run PIMD simulations driven by Deep Potential (DP) models trained on data from density functional theory (DFT) based on SCAN, revPBE0-D3, SCAN0, and revPBE-D3 and a DP model trained on the MB-pol potential. We calculate the  $T_m$  of ice, the density discontinuity at melting, and the temperature of density maximum ( $T_{dm}$ ) of the liquid. We find that the model based on MB-pol agrees well with experiment. The models based on DFT incorrectly predict that NQEs lower  $T_m$ . For the density discontinuity, SCAN and SCAN0 predict values close to the experimental result, while revPBE-D3 and revPBE0-D3 significantly underestimate it. Additionally, the models based on SCAN and SCAN0 correctly predict that the  $T_{dm}$  is higher than  $T_m$ , while those based on revPBE-D3 and revPBE0-D3 predict the opposite. We attribute the deviations of the DFT-based models from experiment to the overestimation of hydrogen bond strength. Our results set the stage for more accurate simulations of aqueous systems grounded on DFT.

## I. INTRODUCTION

Water is arguably the most important substance on Earth. Its rich phase diagram and numerous anomalous properties continue to motivate extensive research efforts [1]. Over the past decades, simulations based on first-principles electronic-structure methods such as density functional theory (DFT) have been widely applied to the study of water. These approaches have successfully reproduced and elucidated many of its structural, thermodynamic, electronic, and transport properties, including the density, radial and angular distribution functions, X-ray absorption spectra, and diffusion coefficients [2–11].

Many problems of interest, however, require long-time simulations of large systems, rendering direct first-principles simulations prohibitively expensive. Examples include predicting the melting properties of ice [12, 13], the phase diagram of water over a broad range of pressures and temperatures [14–16], computing the p $K_w$  of liquid water [17], and estimating ice nucleation rates in deeply supercooled water [18]. The advent of machine-learning potentials (MLPs) [19–24] has revolutionized first-principles simulations, extending accessible time and length scales and enabling computations of properties that were previously infeasible at *ab initio* accuracy.

Among these properties, the thermodynamics of water in the vicinity of the freezing point is of extensive interest [18]. Nuclear quantum effects (NQEs), arising from the light mass

of hydrogen atoms, make a difference on the properties of water at relatively low temperatures. Experimentally, NQEs manifest as an isotope effect in the melting temperature of H<sub>2</sub>O, which is approximately 4 K below that of D<sub>2</sub>O [25]. While NQEs can be included in *ab initio* path integral molecular dynamics (PIMD) simulations [26], the computational cost of DFT-driven PIMD prohibits its use for studying the melting properties of water. MLPs overcome this limitation, enabling long PIMD simulations with explicit NQEs [13, 14, 27, 28].

However, modeling aqueous systems with MLPs remains challenging. Both the underlying electronic-structure methods and the machine learning models themselves require careful validation. On the one hand, the choice of first-principles method is still under debate: different levels of theory exhibit distinct strengths and limitations. For example, DFT with SCAN yields a reasonable density difference between water and ice, but it overestimates the hydrogen bond strength [9, 17], leading to an overstructured liquid. The MB-pol potential reproduces many thermodynamic properties of water in good agreement with experiment [29], but the phase diagram predicted based on MB-pol is currently limited to the low-pressure region [27]. On the other hand, MLPs trained on the same functional can also yield inconsistent predictions. For example, different equilibrium densities have been reported for water using MLPs trained on revPBE0-D3 [13, 14, 30, 31]. One model overestimated the liquid density [31], another obtained a value close to experiment [30], while yet another underestimated it [13]. In principle, different MLPs grounded in the same electronic structure method should produce consistent predictions for the properties of water. These inconsistencies underscore the need for careful validation of both the

\* yifanl0716@gmail.com

† rcar@princeton.edu

training datasets and the associated training protocols.

The goal of this work is to provide a rigorous comparison and validation of MLPs trained on MB-pol and several DFT functionals by assessing their ability to describe properties of water relevant to the melting of ice. This article serves as the accompanying paper to our Letter. In addition to the systematic benchmark of first-principles-based MLPs for water presented therein, we provide full descriptions of the computational methodologies employed, along with more comprehensive results, validations, and comparisons with previous studies.

The remainder of the paper is organized as follows. Section II describes the computational methodology used in this work. Section III reports results from five Deep Potential (DP) models based on different levels of theory. The temperature of density maximum ( $T_{dm}$ ) of liquid water is determined from the density isobars. We also calculate the melting point ( $T_m$ ) and especially discuss how each model captures NQEs on  $T_m$  of water. We then discuss the role of NQEs on the structure of water by analyzing the radial distribution functions (RDFs). In Section IV, we compare our models to published MLPs trained at the revPBE0-D3 level of theory, attributing observed discrepancies to differences in the training set composition. We present concluding remarks in Section V.

## II. METHODOLOGY

In this section, we describe the computational methods adopted in this work. Throughout the paper, we use the superscript “cl” to indicate observables calculated with molecular dynamics (MD) with classical atomic nuclei, and no superscript for path integral molecular dynamics (PIMD) (we use “qu” for PIMD when required to prevent any ambiguity). We use the notation “@” to specify the reference level for each MLP model. For example, DP@SCAN indicates the DP model trained on SCAN data.

### A. DFT Calculations

We train MLPs for four DFT functionals: revPBE-D3 [32, 33], revPBE0-D3 [32–34], SCAN [3], and SCAN0 [35].

Quantum Espresso (QE) [36, 37] v7.0 is used for revPBE-D3 and SCAN calculations. The revPBE-D3 functional is implemented in QE, whereas SCAN is implemented in LIBXC v5.2.2 [38, 39] which is interfaced with QE. For both functionals, we perform plane-wave calculations with kinetic energy cutoffs of 110 Ry for the wave functions and 440 Ry for the charge density. We use Optimized Norm-Conserving Vanderbilt (ONCV) scalar-relativistic pseudopotentials for O and H parametrized using the PBE functional [40]. Only the  $\Gamma$  point of the Brillouin zone is sampled, and the convergence threshold for the self-consistent procedure is set to  $10^{-6}$  Ry.

CP2K [41] v2022.1 is used for revPBE0-D3, which includes 25% exact exchange. The CP2K input file is obtained from the GitHub repository [42], which provides the input files and models used in Ref. [43]. The auxiliary density

matrix method [44] is used to accelerate the Hartree-Fock exchange calculation, and the dual-space Goedecker-Teter-Hutter (GTH) pseudopotentials are used to represent the core electrons. All computational settings follow Refs. [10, 13], except that the plane-wave cutoff energy was increased to 800 Ry for improved convergence. For both revPBE-D3 and revPBE0-D3, we employ the zero-damping variant of Grimme’s D3 dispersion correction, which is the default implementation in QE and CP2K.

For the SCAN0 functional, we use the liquid water training dataset of Ref. [45] and add to it additional ice configurations. SCAN0 includes 10% exact exchange. QE v5.1.1 is used for the calculations. We use the Hamman-Schlüter-Chiang-Vanderbilt (HSCV) pseudopotentials [46, 47] with a wavefunction kinetic energy cutoff of 150 Ry and a charge density cutoff of 600 Ry. All settings for SCAN0 follow Ref. [45].

We used the same pseudopotentials adopted in previous work, namely ONCV for revPBE-D3 and SCAN [12], GTH for revPBE0-D3 [10, 13], and HSCV for SCAN0 [45]. All of these pseudopotentials were constructed from atomic calculations based on the PBE functional and are therefore not fully consistent with the functional used in our condensed phase calculations. Comparisons with all-electron calculations for reference systems support that this inconsistency should have a negligible effect on the properties of water relevant to ice melting.

### B. *Ab Initio* Molecular Dynamics

For the revPBE0-D3 functional, we calculate the densities of water and ice by running *ab initio* molecular dynamics (AIMD) simulations with 64 H<sub>2</sub>O molecules using CP2K v2022.1 [41]. All computational settings for revPBE0-D3 DFT follow those described in Subsection II A and Ref. [13]. We run Born-Oppenheimer molecular dynamics with a timestep of 2 fs in the *NpT* ensemble at 300 K and 1 bar. The masses of both O and H are set to 16 a.u., the physical mass of O. We use a Nosé-Hoover chain thermostat with a chain length of three and a damping time of 160 fs, along with an isotropic barostat with a damping time of 800 fs. The choice of simulation mass does not affect the statistics of thermodynamic properties, such as density.

We also run AIMD simulations of liquid water in the *NVT* ensemble and calculate the density of water from an interpolated  $P(\rho)$  equation of state, as adopted in Ref. [48]. The masses and timestep are chosen the same as in the *NpT* simulations. We employ a Nosé-Hoover chain thermostat with a chain length of three and a damping time of 400 fs. We run AIMD simulations at 300 K and densities  $\rho = 0.7, 0.75, 0.8, 0.85, 0.9, 0.95$ , and  $1.0 \text{ g/cm}^3$ . The internal pressure  $P$  is computed as the average of the diagonal elements of the stress tensor  $\sigma$ :

$$P = \frac{1}{3}(\sigma_{xx} + \sigma_{yy} + \sigma_{zz}) \quad (1)$$

where  $\sigma$  includes contributions from both kinetic energy and ground-state electronic structure calculations. A quartic poly-

nomial is then fitted to the  $P(\rho)$  relation. The density corresponding to  $P = 1$  bar is the equilibrium density at 300 K and 1 bar.

### C. Machine Learning Potentials for Water and Ice

We train the DP models using DeePMD-kit [20, 21] with the se\_e2\_a descriptor [19, 49, 50] with a 6 Å cutoff radius. The training dataset for the DP models based on revPBE-D3, SCAN, and revPBE0-D3 consists of liquid water and hexagonal ice configurations of a 64-molecule cell. In the case of the SCAN0-based model we also included in the training a 96-molecule cell, to be consistent with Ref. [45]. The configurations were generated from classical MD and bead trajectories from PIMD with 32 beads.

For each DFT functional, we train a DP model with an active learning procedure [51] using the DP-GEN software [52], which is a well-established iterative protocol to generate the training dataset for DP models. In this process, each iteration consists of three steps: exploration, labeling, and training. Initially, 4 DP models are trained on a set of 100 configurations of liquid water. In the exploration stage, classical MD and PIMD in the  $NpT$  ensemble are used to explore the configuration space. The “fix npt” module of LAMMPS [53, 54] is used to perform classical MD, and the “fix pimd/langevin” module of LAMMPS is used to perform PIMD with 32 beads. All simulations in the exploration stage are performed at 1 bar. The temperatures of the exploration stage range from 270 K to 350 K for liquid water and from 150 K to 300 K for ice. The maximal standard deviation of the atomic force predicted by the model ensemble, which is often called the *model deviation* for short, is used as the error indicator for a specific configuration. The lower and upper bounds of the trust levels of the model deviation are chosen to be 0.2 and 0.35 eV / Å, respectively. We refer the readers to Ref. [51, 52] for more details about the DP-GEN procedure. The dataset is considered to be converged if the ratio of accurate configurations during the exploration stage is greater than 99.9%, and a DP model trained on this converged dataset is used in the production run.

For MB-pol, we use the DP model trained in Ref [27] which accurately describes the phase diagram of water.

The models and datasets can be found in our GitHub repository [55]. The composition of the training datasets and the training errors can be found in Section ?? of the supplemental material (SM).

### D. Classical and Path Integral Molecular Dynamics

We run MD simulations driven by the 5 DP models based on DFT and MB-pol. All MD and PIMD simulations are done with LAMMPS [53, 54] using a timestep of 0.5 fs. The PIMD simulations are performed with the “fix pimd/langevin” module of LAMMPS. We use 432 H<sub>2</sub>O molecules in all DP-based simulations except for mass thermodynamic integration (128) and quantum direct coexistence (588) calculations. The temperature is controlled using the Nosé-Hoover chain thermostat

with a damping time of 0.1 ps, and the pressure is controlled using the Martyna-Tobias-Klein barostat with a damping time of 0.5 ps. In all PIMD, the temperature is controlled using a local path integral Langevin equation (PILE\_L) thermostat [26] with a damping time of 0.1 ps, and the pressure is controlled with the Bussi-Zykova-Parrinello (BZP) barostat [56] with a damping time of 0.5 ps. We use 32 beads for all PIMD simulations except varying numbers for the mass thermodynamic integration. The densities of classical and quantum ice and water at different temperatures are computed with MD and PIMD simulations in the  $NpT$  ensemble at 1 bar. The temperature of density maximum ( $T_{dm}$ ) of water is found from the density isobars. For the density of water, we use trajectories of 2 ns. For the density of ice, the trajectories span 0.5 ns. The RDFs are calculated in the  $NpT$  ensemble at 1 bar with 1-ns-long trajectories.

### E. Thermodynamic Integration for Classical Free Energy

We first calculate the chemical potentials of classical ice and water and find  $T_m^{cl}$ . The chemical potentials (Gibbs free energy per molecule) of classical water and ice are calculated according to the thermodynamic integration (TI) procedure described in Ref. [15] and below. We model water and ice with 432 H<sub>2</sub>O molecules in a periodic cell and use LAMMPS [53] [54] interfaced with DeePMD-kit for all the TI tasks generated by the software package DPTI [57]. The Simpson rule is used to calculate all the numerical integrals.

The TI protocol consists of four steps:

- Step 1:  $NpT$  equilibrium simulation.
- Step 2:  $NVT$  equilibrium simulation.
- Step 3: Hamiltonian thermodynamic integration (HTI) at fixed volume.
- Step 4: TI along a temperature path at constant pressure.

#### Step 1: $NpT$ Equilibrium Simulation

In the first step, the  $NpT$  simulation, one calculates the equilibrium density of the system, which will be used in the Hamiltonian TI step. The  $NpT$  run spans 1 ns. The temperature is  $T_{init} = 150$  K for ice and  $T_{init} = 300$  K for water and is controlled with a Nosé-Hoover chain thermostat with a damping time of 0.1 ps. The pressure is  $P = 1$  bar and kept constant with a Martyna-Tobias-Klein barostat with a damping time of 0.5 ps. The corresponding equilibrium volume  $V_{eq}$  is used in the next 2 steps.

#### Step 2: $NVT$ Equilibrium Simulation

In the second step,  $NVT$  simulations are performed at the equilibrium density obtained in Step 1 to generate equilibrium configurations of ice and water, which are then used as the

initial configurations for Step 3. The  $NVT$  runs span 100 ps. The systems are kept at the equilibrium volume  $V_{\text{eq}}$  calculated in Step 1. The temperature is kept at  $T_{\text{init}}$  with a Nosé-Hoover chain thermostat with a damping time of 0.1 ps.

### Step 3: Hamiltonian Thermodynamic Integration

Hamiltonian Thermodynamic Integration (HTI) is used to compute the Helmholtz free energy relative to a reference state for which the free energy can be calculated analytically. For each phase  $\alpha$ , the relative free energy is calculated by

$$A_\alpha - A_0 = \int_0^1 \langle U_\alpha - U_0 \rangle_\lambda d\lambda. \quad (2)$$

where  $A_\alpha$  and  $A_0$  are the Helmholtz free energies of the target and reference states, respectively, and  $U_\alpha$  and  $U_0$  are the corresponding potential energies.  $\langle \cdot \rangle_\lambda$  is the ensemble average for the interpolated potential

$$U(\lambda) = (1 - \lambda)U_0 + \lambda U_\alpha. \quad (3)$$

The reference states for liquid water and ice are an ideal gas of non-interacting water molecules with harmonic bonds and an atomic Einstein crystal, respectively. To ensure reversibility of the HTI path, two intermediate states are introduced along each integration path. For ice, a soft-core Lennard-Jones (LJ) interaction is added onto the Einstein crystal; the DP potential is then gradually turned on; and finally, the harmonic and soft-core LJ potentials are switched off. For liquid water, a harmonic angle term and a soft-core LJ interaction are added onto the ideal-gas reference; the DP potential is then turned on; and finally, the harmonic bond and angle terms, together with the soft-core LJ interaction, are turned off. Additional details can be found in the Supplemental Material of Ref. [15].

The corresponding Gibbs free energies  $G_\alpha$  are obtained from the Helmholtz free energies  $A_\alpha$  by  $G_\alpha = A_\alpha + PV_{\text{eq}}$ , where  $P = 1$  bar and  $V_{\text{eq}}$  is the equilibrium volume obtained in Step 1. The classical chemical potentials are  $\mu_\alpha^{\text{cl}} = \frac{G_\alpha}{N_{\text{H}_2\text{O}}}$ , where  $N_{\text{H}_2\text{O}}$  is the number of water molecules.

The interpolated potential  $U(\lambda)$  is evaluated using the “fix adapt/fep” feature of LAMMPS. In HTI for ice we keep the temperature at  $T_{\text{init}} = 150$  K using a Langevin thermostat with a damping time of 0.1 ps. In HTI for water we keep the temperature at  $T_{\text{init}} = 300$  K using a Nosé-Hoover chain thermostat with a damping time of 0.1 ps. MD simulation at each  $\lambda$  spans 500 ps.

### Step 4: Thermodynamic Integration along a Temperature Path

From the chemical potentials  $\mu(P, T_{\text{init}})$  calculated at  $T_{\text{init}}$  in Step 3, the chemical potentials at the target temperatures  $T$  are calculated with the formula [15]

$$\frac{\mu_\alpha^{\text{cl}}(P, T) - \mu_\alpha^{\text{cl}}(P, T_{\text{init}})}{k_B T} = \int_{T_{\text{init}}}^T \frac{1}{N_{\text{H}_2\text{O}} k_B T'^2} \langle U + PV \rangle_{P, T'} dT' \quad (4)$$

where  $U$  is the potential energy evaluated by the DP models,  $V$  is the volume and  $\langle \cdot \rangle_{P, T'}$  is the ensemble average in the  $NpT$  ensemble at pressure  $P$  and temperature  $T'$ . The free energy difference between classical ice and water is then calculated as  $\Delta\mu_{\text{ice}-\text{liq}}^{\text{cl}}(T) = \mu_{\text{ice}}^{\text{cl}}(T) - \mu_{\text{liq}}^{\text{cl}}(T)$ .

We run an MD in the  $NpT$  ensemble at temperature increments of 5 K, spanning 150–350 K for ice and 250–350 K for water. Each simulation is run for 500 ps. The temperature is kept constant using the the Nosé-Hoover chain with a damping time of 0.1 ps. The pressure is maintained using the Martyna-Tobias-Klein barostat with a damping time of 0.5 ps.

To check the correctness of TI in the Step 4 we repeat Steps 1 to 3 at an additional temperature, namely  $T_{\text{init}} = 300$  K for ice and  $T_{\text{init}} = 350$  K for water.

## F. Thermodynamic Integration for Quantum Free Energy

We add the quantum correction to the chemical potentials using the mass thermodynamic integration (MTI) method and find  $T_m$ . The quantum correction to  $\mu_\alpha^{\text{cl}}(T)$  for phase  $\alpha$  is [13, 27, 58]:

$$\Delta\mu_\alpha^{\text{qu-cl}}(T) = \mu_\alpha(T) - \mu_\alpha^{\text{cl}}(T) = \int_0^1 g_\alpha(y) dy, \quad (5)$$

where  $g_\alpha(y)$  is defined by

$$g_\alpha(y) = 2 \frac{\langle K_{\text{CV}, \alpha} \left( \frac{m}{y^2 \hbar^2} \right) \rangle - \frac{3Nk_B T}{2N_{\text{H}_2\text{O}}}}{y}. \quad (6)$$

The centroid-virial estimator  $K_{\text{CV}, \alpha} \left( \frac{m}{y^2 \hbar^2} \right)$  for phase  $\alpha$  is calculated from PIMD simulations with atomic masses scaled with  $1/y^2$  as

$$K_{\text{CV}} = \frac{3Nk_B T}{2N_{\text{H}_2\text{O}}} - \frac{1}{2nN_{\text{H}_2\text{O}}} \sum_{k=1}^n \sum_{i=1}^N \left( \mathbf{r}_i^{(k)} - \mathbf{r}_i^{(c)} \right) \cdot \mathbf{F}_i^{(k)} \quad (7)$$

where  $N$  is the number of atoms,  $T$  is the temperature,  $n$  is the number of beads,  $\mathbf{r}_i^{(k)}$  and  $\mathbf{F}_i^{(k)}$  are the coordinates and forces of the  $k$ -th bead of the  $i$ -th atom, respectively, and  $\mathbf{r}_i^{(c)} = \frac{1}{n} \sum_{k=1}^n \mathbf{r}_i^{(k)}$  is the centroid of the beads for atom  $i$ .

We refer the readers to Appendix A for the derivation of Eqs. (5) and (6). In practice, we first calculate

$$\Delta g_{\text{ice}-\text{liq}}(y) = g_{\text{ice}}(y) - g_{\text{liq}}(y) \quad (8)$$

from PIMD with  $y = 0.1, 0.2, 0.3, 0.4, 0.6, 1.0$ . For each value of  $y$ , we perform PIMD simulations of ice and water in a periodic box containing 128 molecules, using 8, 16, 32, 64, 64, and 64 beads, respectively. The simulations are carried out with the “fix pimd/langevin” feature of LAMMPS [53, 54]. Each PIMD run is conducted in the  $NpT$  ensemble for 500 ps using a timestep of 0.5 fs. We then perform the integration

$$\Delta\mu_{\text{ice}}^{\text{qu-cl}}(T) - \Delta\mu_{\text{liq}}^{\text{qu-cl}}(T) = \int_0^1 \Delta g_{\text{ice}-\text{liq}}(y) dy \quad (9)$$

using the trapezoidal rule on the grid of  $y = 0.0, 0.1, 0.2, 0.3, 0.4, 0.6, 1.0$ . The quantum free energy difference is thus calculated as  $\Delta\mu_{\text{ice}-\text{liq}}^{\text{qu}}(T) = \Delta\mu_{\text{ice}}^{\text{qu}-\text{cl}}(T) - \Delta\mu_{\text{liq}}^{\text{qu}-\text{cl}}(T) + \Delta\mu_{\text{ice}-\text{liq}}^{\text{cl}}(T)$ .

For DP@revPBE-D3 and DP@revPBE0-D3, PMID simulations are performed at temperatures at 10 K intervals, ranging from 270 K to 330 K. For DP@SCAN and DP@SCAN0, PMID simulations are performed at temperatures at 10 K intervals, ranging from 300 K to 330 K. The temperatures are kept constant using a PILE\_L thermostat with a damping time of 0.1 ps, and the pressure is controlled with the Bussi-Zykova-Parrinello barostat [56] with a damping time of 0.5 ps.

### G. Quantum Direct Coexistence Simulations

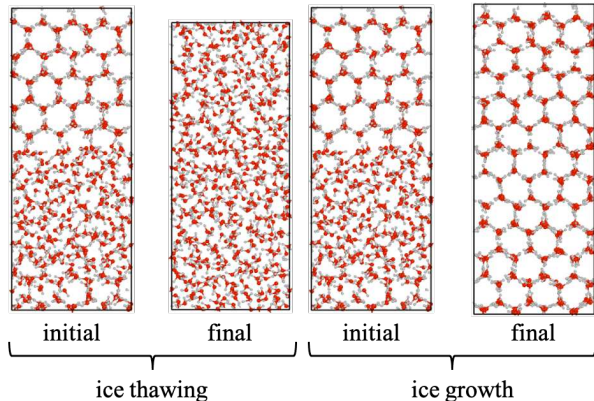


FIG. 1. The initial and final states of the direct coexistence simulation are demonstrated. The coexisting ice and water system tend to thaw at high temperatures, and ice grows at low temperatures.

To independently assess the accuracy of our thermodynamic integration approach we also calculate the melting point of quantum ice with the direct coexistence method for DP@SCAN. We run the water-ice Ih coexistence simulations using PIMD with 576 molecules and 32 beads in the  $NpT$  ensemble at 6 temperatures: 320 K, 321.5 K, 323 K, 325 K, 327 K, and 330 K. Temperature is kept constant using the PILE\_L thermostat [26] with a relaxation time of 0.1 ps. Pressure is kept at 1 bar using the BZP barostat [56] with a relaxation time of 0.5 ps. Configurations of ice Ih with proton disorder are obtained with the GenIce software [59]. As illustrated in FIG. 1, the primary prismatic plane ( $10\bar{1}0$ ) of ice Ih is exposed to the liquid. The sides of the box perpendicular to ( $10\bar{1}0$ ) are fixed to the equilibrium values of the DP model, while the side of the box parallel to ( $10\bar{1}0$ ) is allowed to fluctuate to keep the pressure at 1 bar. Five PIMD simulations are performed at each temperature with different random seeds for the stochastic thermostat.

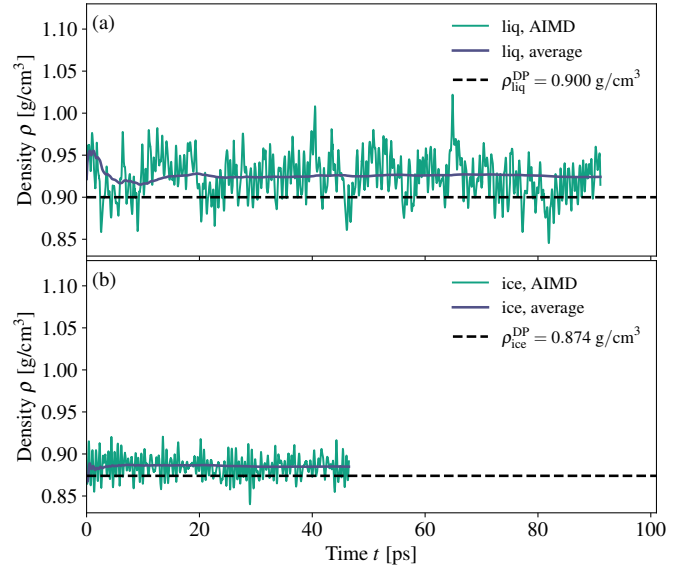


FIG. 2. The density along trajectories of (a) liquid water and (b) ice from AIMD simulations in the  $NpT$  ensemble. The green lines are the densities and the purple lines are the accumulated averages of the densities. The black dash lines are the average densities calculated from MD simulations of 64 H<sub>2</sub>O molecules driven by DP models.

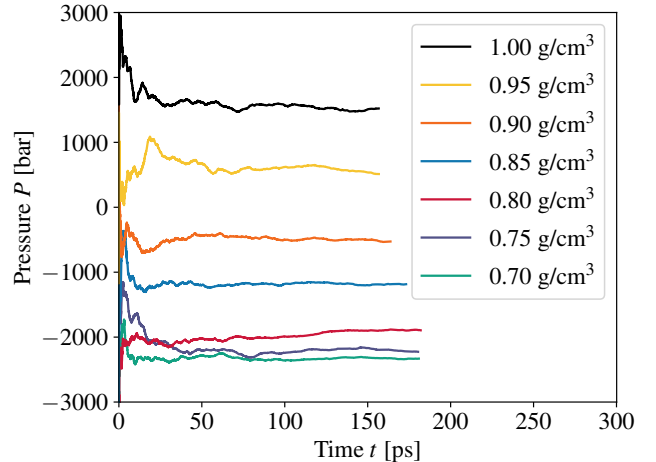


FIG. 3. Accumulated averages of the internal pressure  $P$  from AIMD simulations of water with 64 H<sub>2</sub>O molecules in the  $NVT$  ensemble at 300 K and different densities.

## III. RESULTS AND DISCUSSIONS

In this section, we present the calculated properties of water obtained from our simulations. We first report results from AIMD and compare them with those from DPMD, followed by properties that are accessible only through DPMD.

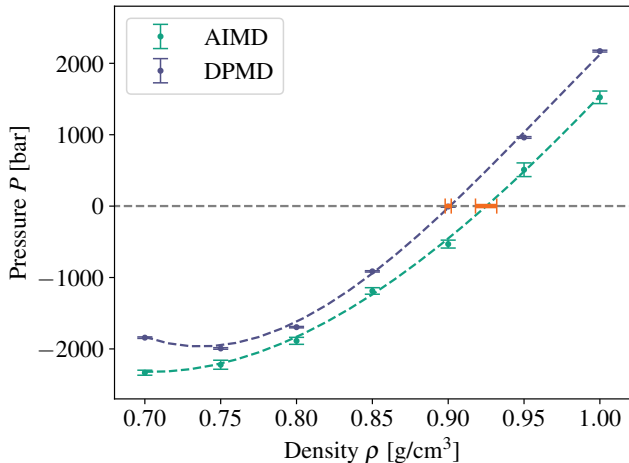


FIG. 4. Average internal pressure  $P$  from AIMD and DPMD simulations of water in the  $NVT$  ensemble at different densities  $\rho$ . A quartic polynomial is fitted to the  $P(\rho)$  equation of state. The gray dashed line corresponds to the pressure 1 bar. The equilibrium density at 300 K and 1 bar determined from the polynomial is shown in orange, which is  $0.925 \pm 0.007$  and  $0.900 \pm 0.002$  g/cm<sup>3</sup> from AIMD and DPMD simulations, respectively.

### A. Density from *Ab Initio* Molecular Dynamics

We plot the densities of water and ice calculated by the  $NpT$  AIMD simulations in FIG. 2. The density of liquid water has a large fluctuation and the  $\sim 100$ -ps-long trajectory gives  $0.925 \pm 0.020$  g/cm<sup>3</sup>, slightly higher than the  $0.900 \pm 0.003$  g/cm<sup>3</sup> calculated by the  $NpT$  DPMD of 64 H<sub>2</sub>O molecules. The AIMD simulation predicts the density of ice to be  $0.887 \pm 0.015$  g/cm<sup>3</sup>, also slightly higher than the  $0.874 \pm 0.002$  g/cm<sup>3</sup> calculated by the  $NpT$  DPMD. The density discontinuity calculated by AIMD is  $0.038 \pm 0.025$  g/cm<sup>3</sup>, a little bit larger compared to the  $0.026 \pm 0.004$  g/cm<sup>3</sup> calculated by the  $NpT$  DPMD. The densities calculated by DPMD and AIMD are comparable with each other within statistical uncertainty. A possible way of reducing the density deviation of DPMD relative to AIMD is to include the virial tensor in the training of the model [19].

We report the accumulated averages of the internal pressures  $P$  at various densities calculated with AIMD simulations in FIG. 3. The average internal pressures as a function of densities are plotted in FIG. 4. For comparison, we also plot the internal pressures calculated with DPMD simulations in FIG. 4. The densities of water from this approach are  $0.923 \pm 0.01$  g/cm<sup>3</sup> for AIMD and  $0.900 \pm 0.002$  g/cm<sup>3</sup> for DPMD, respectively. The densities from the  $NVT$  simulations are in good agreement with the results of the  $NpT$  simulations reported above. As illustrated in FIG. 4, the DP model systematically overestimates the values of the internal pressure, leading to an underestimated density. This observation is consistent with the underestimated densities of water and ice from the DPMD simulations in the  $NpT$  ensemble.

### B. Density Isobars of Water and Ice

We report the density isobars of classical and quantum water and ice in FIG. 5. For comparison, we also plot the  $T_m$  reported in the following subsections.  $T_{dm}$  is found from the density curves and listed in TABLE I.

TABLE I. Temperature of density maximum ( $T_{dm}$ ) of classical and quantum water

Model	$T_{dm}^{cl}$ [K]	$T_{dm}$ [K]
Experiment [25]		277.13
DP@MB-pol	268	271
DP@revPBE0-D3	282	285
DP@revPBE-D3	299	308
DP@SCAN0	326	339
DP@SCAN	324	340

As shown in FIG. 5, NQEs change the densities of water and ice slightly, making a difference of only 1% to 2%. DP@MB-pol slightly overestimates the density of water and makes a good prediction for ice, leading to a slightly overestimated density discontinuity between water and ice. DP@SCAN and DP@SCAN0 overestimate the densities of water and ice by about 4%, and the density discontinuity is slightly underestimated compared to experiment. DP@revPBE-D3 and DP@revPBE0-D3 underestimate the density of water significantly while only slightly underestimating the density of ice, resulting in an underestimated discontinuity.

DP@MB-pol and DP@revPBE0-D3 predict  $T_{dm}$  in relatively good agreement with experiment, whereas DP@SCAN and DP@SCAN0 overestimate it. More importantly, when compared to the predicted  $T_m$ , DP@MB-pol, DP@SCAN, and DP@SCAN0 predict  $T_{dm} > T_m$ , consistent with experiment, while overestimating the magnitude of  $T_{dm} - T_m$ . In contrast, DP@revPBE-D3 and DP@revPBE0-D3 predict  $T_{dm} < T_m$ .

### C. Classical Chemical Potentials and Melting Temperatures

We report the chemical potentials of the classical water and ice in FIG. 6. To verify the correctness of TI, we repeat Step 3, the HTI calculations at two different temperatures  $T_{init}$  for each phase: 150 K and 300 K for ice, and 300 K and 350 K for water. The  $\mu_\alpha^{cl}(T_{init})$  values from these HTI calculations can be found in Section ?? of the SM. Then we start from  $\mu_\alpha^{cl}(T_{init})$  and perform Step 4, the TI along a temperature path. The  $\mu_\alpha^{cl}(T)$  curves from different  $T_{init}$  values agree with each other, validating the correctness of the TI calculations. The temperature where  $\mu_{ice}^{cl}(T) = \mu_{liq}^{cl}(T)$  is determined to be  $T_m^{cl}$  of the classical ice, as listed in TABLE II.

### D. Quantum Chemical Potentials and Melting Temperatures

In FIG. 7, we plot  $\Delta g_{ice-liq}(y)$  as defined by Eq. (8), which is the integrand of MTI in Eq. (9), at temperatures close to the  $T_m^{cl}$  of each model. The  $\Delta g_{ice-liq}(y)$  curves at different

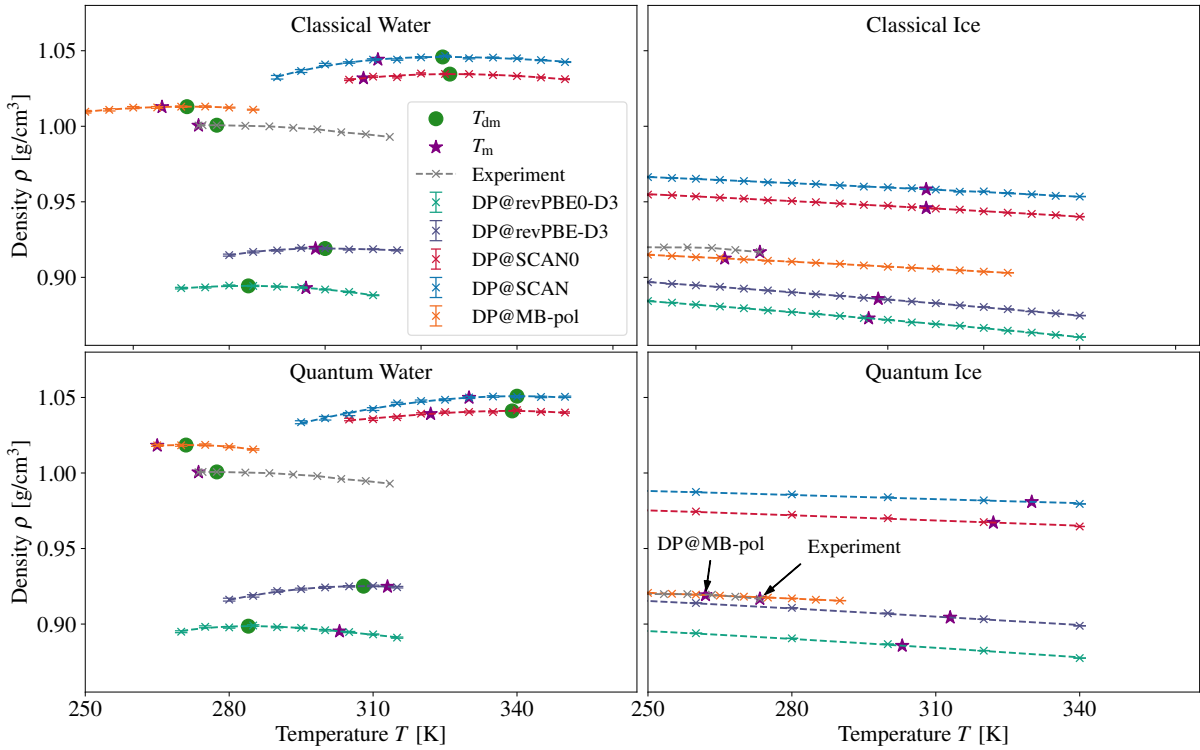


FIG. 5. Density isobars of classical and quantum water and ice. The densities are calculated with classical MD and PIMD simulations in the  $NpT$  ensemble at 1 bar.  $T_{dm}$  represents the temperature of density maximum of water.  $T_m$  represents the melting temperature of ice.

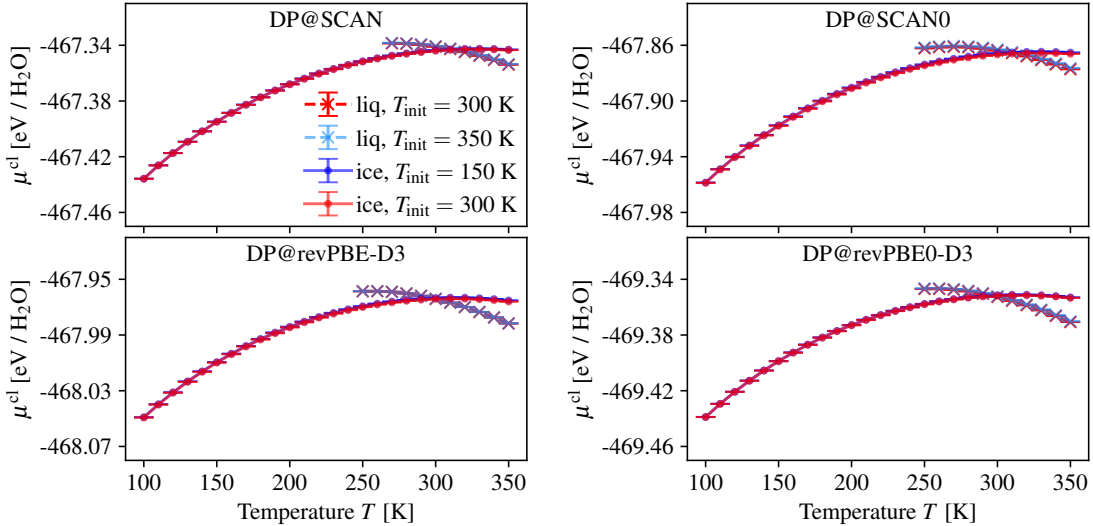


FIG. 6. Classical chemical potential  $\mu^{cl}$  of ice and water calculated by the thermodynamic integration (TI) along the temperature path.  $T_{init}$  is the temperature where the Hamiltonian thermodynamic integration (HTI) is performed. The free energy curves of a specific phase calculated with the same model calculated with different  $T_{init}$  agree with each other, demonstrating the correctness of the TI calculation.

temperatures for the DFT-based DP models can be found in Section ?? of the SM. Interestingly,  $\Delta g_{ice-liq}(y)$  changes sign within the range  $y \in (0, 1)$ , indicating that the value of the integral depends on a cancellation between negative (−) and positive (+) contributions. We plot the resulting  $\Delta\mu_{ice}^{qu-cl}(T) -$

$\Delta\mu_{liq}^{qu-cl}(T)$  in FIG. 8. A negative  $\Delta\mu_{ice}^{qu-cl}(T) - \Delta\mu_{liq}^{qu-cl}(T)$  means that ice is stabilized relative to water by NQE, and correspondingly  $T_m > T_m^{cl}$ . We see in FIG. 7 that only DP@MB-pol has the right qualitative behavior, i.e.,  $T_m < T_m^{cl}$ .  $T_m - T_m^{cl}$ , which is incorrectly predicted to be positive, gets larger

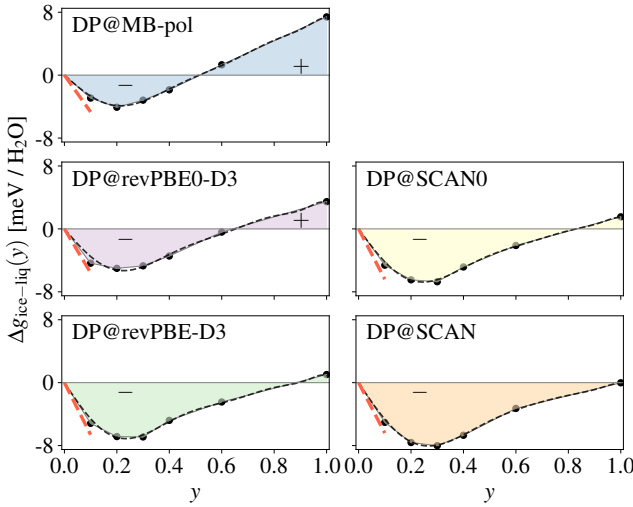


FIG. 7. Integrand  $\Delta g_{\text{ice-liq}}(y)$  of MTI. Regions with  $\Delta g_{\text{ice-liq}}(y) > 0$  and  $< 0$  are labeled “+” and “−”, respectively; a larger “+” region indicates  $\Delta T_m^{\text{qu-cl}} < 0$ . Results for DP@MB-pol are computed at 270 K, while those for the four DFT-based models are computed at 300 K (close to the  $T_m^{\text{cl}}$  of each model). Black dots denote the  $y$  values at which PIMD simulations are performed. Red dashed lines show the slopes  $d\Delta g_{\text{ice-liq}}(y)/dy|_{y=0}$  predicted by the perturbative expansion of  $\Delta\mu_{\text{ice}}^{\text{qu-cl}}(T) - \Delta\mu_{\text{liq}}^{\text{qu-cl}}(T)$  up to  $\hbar^2$ . Black dashed lines represent polynomial fits of  $\Delta g(y)$  using odd orders of  $y$  up to  $y^{13}$ , corresponding to an expansion of  $\Delta\mu_{\text{ice}}^{\text{qu-cl}}(T) - \Delta\mu_{\text{liq}}^{\text{qu-cl}}(T)$  in even powers of  $\hbar$  up to  $\hbar^{14}$ .

and larger as we go from DP@revPBE0-D3 to DP@SCAN0, DP@revPBE-D3, and DP@SCAN. We also plot  $\Delta\mu_{\text{ice-liq}}^{\text{cl}}(T)$  and  $\Delta\mu_{\text{ice-liq}}^{\text{qu}}(T)$  in FIG. 8. The melting temperatures found from  $\Delta\mu_{\text{ice-liq}}(T_m) = 0$  are listed in TABLE II. DP@MB-pol underestimates  $T_m$  while the DFT-based models overestimate  $T_m$ . We then report  $T_{\text{dm}} - T_m$  in TABLE III. These results have been discussed in Subsection III B.

TABLE II. Melting point ( $T_m$ ) of classical and quantum ice Ih<sup>a</sup>

	$T_m^{\text{cl}}$ [K]	$T_m$ [K]	$T_m - T_m^{\text{cl}}$ [K]
Experiment [25]	NA <sup>b</sup>	273.15	< -4.49
DP@MB-pol <sup>c</sup>	266.2	262.3	-3.9
DP@revPBE0-D3	296 (1)	303 (1)	+7
DP@revPBE-D3	298 (1)	313 (1)	+15
DP@SCAN0	308 (1)	322 (1)	+14
DP@SCAN	311 (1)	330 (1)	+19

<sup>a</sup> The value in parentheses is the statistical uncertainty in the last digit.

<sup>b</sup> Although classical water does not exist in the real world, we can infer that classical H<sub>2</sub>O should have a  $T_m$  higher than 273.15 K, given that the  $T_m$  of T<sub>2</sub>O and D<sub>2</sub>O are 277.64 K and 276.97 K, respectively.

<sup>c</sup> The data for MB-pol are quoted from Ref. [60].

TABLE III. Difference between  $T_{\text{dm}}$  and  $T_m$

Model	$T_{\text{dm}}^{\text{cl}} - T_m^{\text{cl}}$ [K]	$T_{\text{dm}} - T_m$ [K]
Experiment [25]		+3.98
DP@MB-pol	+2.2	+8.7
DP@revPBE0-D3	-14	-18
DP@revPBE-D3	+1	-5
DP@SCAN0	+18	+17
DP@SCAN	+13	+10

TABLE IV. Density of classical water and ice at  $T_m^{\text{cl}}$

Model	$T_m^{\text{cl}}$ [K]	$\rho_{\text{liq}}^{\text{cl}}$	$\rho_{\text{ice}}^{\text{cl}}$	$\rho_{\text{liq}}^{\text{cl}} - \rho_{\text{ice}}^{\text{cl}}$ [g/cm <sup>3</sup> ]
DP@MB-pol	266	1.013	0.913	0.100
DP@revPBE0-D3	296	0.893	0.873	0.020
DP@revPBE-D3	298	0.919	0.886	0.033
DP@SCAN0	308	1.032	0.946	0.086
DP@SCAN	311	1.044	0.958	0.086

### E. Perturbative Expansion of the Quantum Free Energy

In FIG. ?? of the Letter we show the polynomial fitting of  $g_\alpha(y)$  using odd powers of  $y$  up to  $y^{13}$ . From Eq. (5) we realize that  $g_\alpha(y) = d\Delta\mu_\alpha^{\text{qu-cl}}(T)/dy$ . Since  $\Delta\mu_\alpha^{\text{qu-cl}}(T)$  only depends on even powers of  $\hbar$ ,  $g_\alpha(y)$  can be obtained from a perturbative expansion in odd powers of  $\hbar$  [61–64]. The lowest-order term is of order  $\hbar^2$  and corresponds to the derivative  $\frac{dg_\alpha}{dy}|_{y=0}$ , which has an analytical expression that can be calculated from classical MD simulations:

$$\frac{dg_\alpha}{dy} \Big|_{y=0} = \frac{\hbar^2}{12T^2 N_{\text{H}_2\text{O}}} \sum_i \frac{1}{m_i} \left\langle \|\mathbf{F}_i\|^2 \right\rangle_\alpha^{\text{cl}} \quad (10)$$

where  $T$  is the temperature,  $N_{\text{H}_2\text{O}}$  is the number of water molecules in the classical MD simulations,  $i$  iterates over all atoms in the system,  $m_i$  is the mass of atom  $i$ , and  $\langle \cdot \rangle_\alpha^{\text{ice}}$  is the classical  $NpT$  ensemble average for phase  $\alpha$ .  $\|\mathbf{F}_i\|^2$  is the square of the 2-norm of the force of atom  $i$ . We refer the readers to Appendix B for the derivation of Eq. (10).

The classical  $NpT$  averages can be calculated with classical MD, thus providing an independent check of our PIMD simulations. The slopes calculated from Eq. (10) are reported as red dashed lines in FIG. ?? of the Letter, showing good agreement with the results of PIMD.

In addition, we report in FIG. 7 the polynomial fitting of  $\Delta g_{\text{ice-liq}}(y)$  and the predicted  $\frac{d\Delta g_{\text{ice-liq}}(y)}{dy} \Big|_{y=0}$  calculated using Eq. (10). We see that the numerical derivative estimated from  $\Delta g_{\text{ice-liq}}(y) = 0.1$  is very close to the value obtained from classical simulations, further supporting the accuracy of our approach. We found that in order to reproduce  $\Delta g_{\text{ice-liq}}(y)$  in the interval  $y \in (0, 1)$  with perturbation theory, terms up to  $\hbar^{12}$  need to be included in the expansion, and the fitting can be further improved by including higher orders of  $\hbar$ . We can observe from FIG. 7 that an expansion up to  $\hbar^{13}$  gives very good fitting to  $\Delta g_{\text{ice-liq}}(y)$ . This indicates

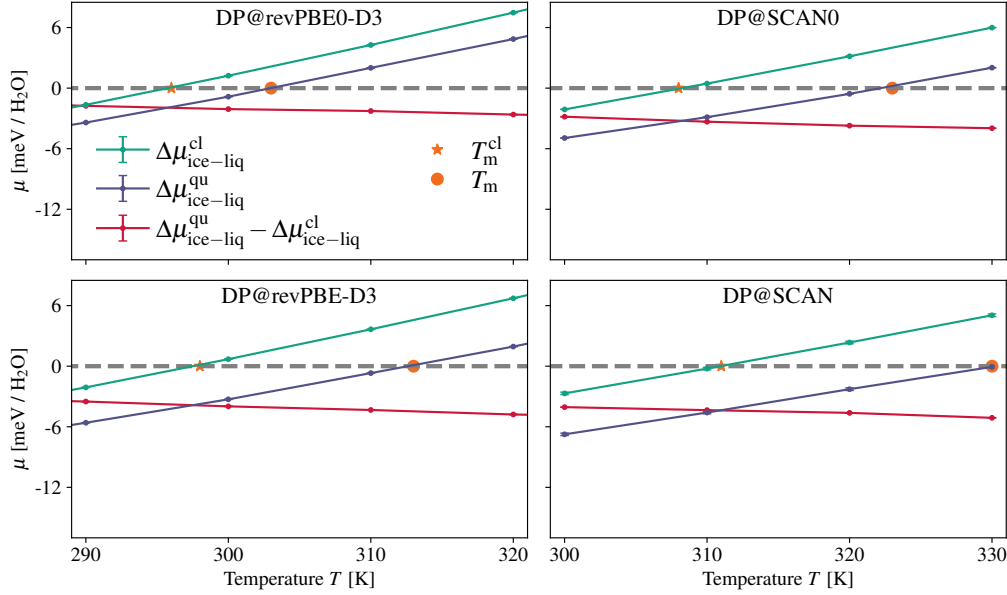


FIG. 8. Chemical potential differences of ice Ih and water as a function of temperature for the DFT-based models. The temperatures where  $\Delta\mu_{\text{ice-liq}}(T) = 0$  are the melting temperatures  $T_m$ .

TABLE V. Density of quantum water and ice at  $T_m$

Model	$T_m$ [K]	$\rho_{\text{liq}}$	$\rho_{\text{ice}}$	$\rho_{\text{liq}} - \rho_{\text{ice}}$ [g/cm <sup>3</sup> ]
Experiment [25]	273.15	0.9998	0.917	0.083
DP@MB-pol	262	1.019	0.919	0.100
DP@revPBE0-D3	303	0.895	0.885	0.010
DP@revPBE-D3	313	0.924	0.906	0.018
DP@SCAN0	322	1.039	0.967	0.072
DP@SCAN	330	1.050	0.981	0.069

that NQEs in water are not small in a perturbative sense. It is only because of cancellation between contributions of different signs that the NQEs on  $T_m$ , or equivalently the isotope effect on it, is rather small. We also compare the integration of the fitted polynomial on  $y \in (0, 1)$  with the integration obtained with the trapezoidal rule, showing that the error introduced by the numerical integration on discrete points of  $y$  is essentially small.

In FIG. 7,  $\Delta g_{\text{ice-liq}}(y)$  is fitted by a polynomial in odd powers of  $y$ , consistent with the theoretical result that the quantum correction to the free energy is given by an expansion in even powers of  $\hbar$ . The dashed lines in FIG. 7 correspond to fittings of  $\Delta g_{\text{ice-liq}}(y)$  according to:

$$\Delta \tilde{g}_{\text{ice-liq}}(y) = \sum_{i=1}^7 a_i y^{2i-1}. \quad (11)$$

To avoid overfitting,  $\Delta g_{\text{ice-liq}}(y)$  is first linearly interpolated on 100 points in an evenly spaced grid in  $y \in (0, 1]$ . Then, the coefficients  $\{a_i\}$  are calculated with least squares regression. Using Eq. (11) the integral  $\int_0^1 \Delta g_{\text{ice-liq}}(y) dy$  can be calcu-

lated analytically as

$$I_2 = \int_0^1 \Delta \tilde{g}_{\text{ice-liq}}(y) dy = \sum_{i=1}^7 \frac{a_i}{2i}. \quad (12)$$

The difference between the integral calculated numerically with the trapezoidal rule ( $I_1$ ) and that calculated with Eq. (12) ( $I_2$ ) is reported in TABLE VI. The differences in TABLE VI are of the order of 0.03 meV / H<sub>2</sub>O or smaller, implying that the integration error of the trapezoidal rule is essentially small.

TABLE VI. The integration of  $\Delta g_{\text{ice-liq}}(y)$  curves in FIG. 7 calculated with the trapezoidal formula ( $I_1$ ) and the analytical integration of the polynomial fit  $\Delta \tilde{g}_{\text{ice-liq}}(y)$  ( $I_2$ )

Model	$T$ [K]	$I_1$	$I_2$	$I_1 - I_2$ [meV / H <sub>2</sub> O]
DP@MB-pol	270	0.59	0.58	0.01
DP@revPBE0-D3	300	-1.32	-1.35	0.03
DP@revPBE-D3	300	-3.13	-3.14	0.01
DP@SCAN0	300	-2.82	-2.83	0.01
DP@SCAN	300	-4.05	-4.06	0.01

## F. Direct Coexistence Simulations

The results of the quantum direct coexistence simulations with DP@SCAN are shown in FIG. 9. At 320 K the ice crystal grows at the expense of liquid water and at 325 K ice thaws. At 321.5 K and 323 K, ice can either grow or melt with the probabilities shown in FIG. 10, indicating that the quantum melting point of ice Ih is  $324 \pm 3$  K.

This is slightly different from the value of  $330 \pm 1$  K obtained with thermodynamic integration using 64 beads for the systems with  $y \geq 0.4$ . As shown in Section ?? of the SM, using only 32 beads when  $y \geq 0.4$  in thermodynamic integration gives  $T_m = 328 \pm 1$  K, consistent with the value obtained with the coexistence method within error bars.

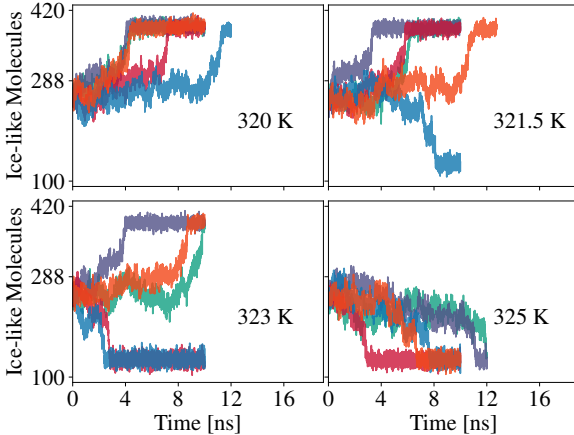


FIG. 9. Number of ice Ih-like molecules [65] as a function of time in the direct coexistence simulation. Five independent runs with different seeds for the stochastic thermostat are shown in different colors at four temperatures.

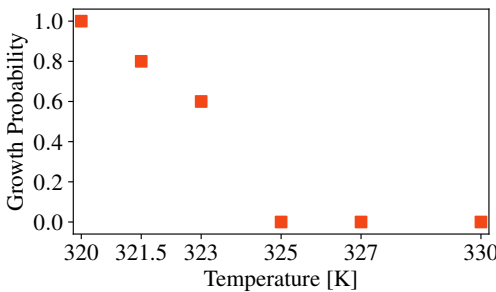


FIG. 10. Ice growth probabilities among the five runs at each simulation temperature. It shows that  $T_m = 324 \pm 3$  K for DP@SCAN.

### G. Radial Distribution Functions of Water

We compare the O–O RDFs of liquid water predicted by DP@SCAN and DP@SCAN0, as well as those predicted by DP@revPBE-D3 and DP@revPBE0-D3, at their respective  $T_m + 25$  K. As shown in FIG. 11, introducing a hybrid functional produces only negligible changes in the water structure. Consequently, the O–O RDF obtained with DP@SCAN in FIG. ?? of the Letter should be nearly identical to that obtained with DP@SCAN0, and the same conclusion holds for DP@revPBE-D3 and DP@revPBE0-D3.

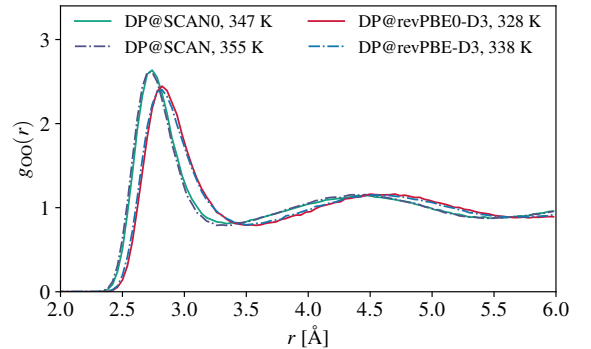


FIG. 11.  $g_{OO}(r)$  of quantum water calculated by DP models at predicted  $T_m + 25$  K. The O–O RDFs calculated by DP@revPBE-D3 and DP@revPBE0-D3 are almost identical, as are those calculated with DP@SCAN and DP@SCAN0.

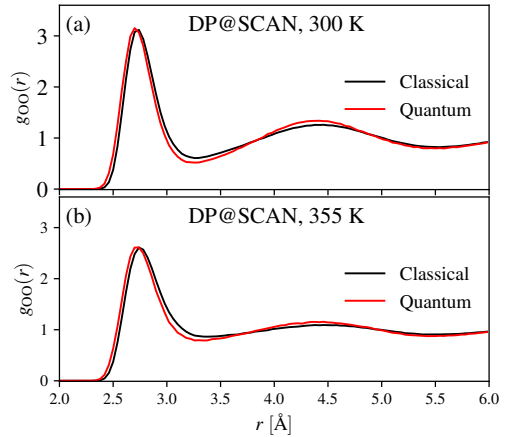


FIG. 12.  $g_{OO}(r)$  of classical and quantum water calculated by DP@SCAN at 300 K and 355 K. When classical and quantum RDFs are compared at the same absolute temperature, the quantum RDF shows an artificial enhancement of the second peak that is not observed experimentally.

We emphasize that comparing classical and quantum water at temperatures measured relative to their respective melting points,  $T_m^{cl}$  and  $T_m$ , is more appropriate than comparing them at the same absolute temperature. As illustrated in FIG. 12, comparing the O–O RDFs of classical and quantum water at 300 K (or 355 K) leads to spurious overstructuring in the first interstitial region and the second peak, which are absent in experiment. In contrast, comparing classical water at  $T_m^{cl} + 25$  K with quantum water at  $T_m + 25$  K avoids these artifacts, as discussed below.

We compare the O–O, O–H, and H–H RDFs of liquid water,  $g_{OO}(r)$ ,  $g_{OH}(r)$ , and  $g_{HH}(r)$  in FIG. 13, FIG. 14, and FIG. 15, respectively. We report the RDFs of classical and quantum water at the corresponding  $T_m^{cl} + 25$  K and  $T_m + 25$  K, respectively, and compare them with the experimental RDFs of  $D_2O$  and  $H_2O$  reported in Ref. [66]. As shown in FIG. 13, the five models predict similar NQE on the  $g_{OO}(r)$ : the first peak

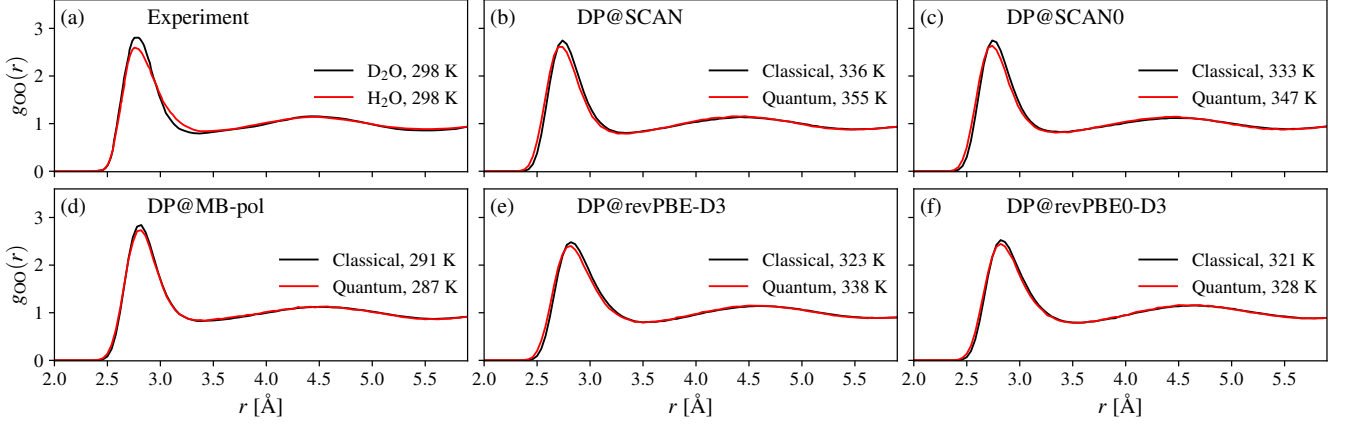


FIG. 13. O-O RDF  $g_{OO}(r)$  of liquid water. (a) Experimental result from [66]. (b)  $g_{OO}(r)$  of classical and quantum water calculated by the models at their predicted  $T_m^{cl} + 25$  K and  $T_m + 25$  K, respectively.

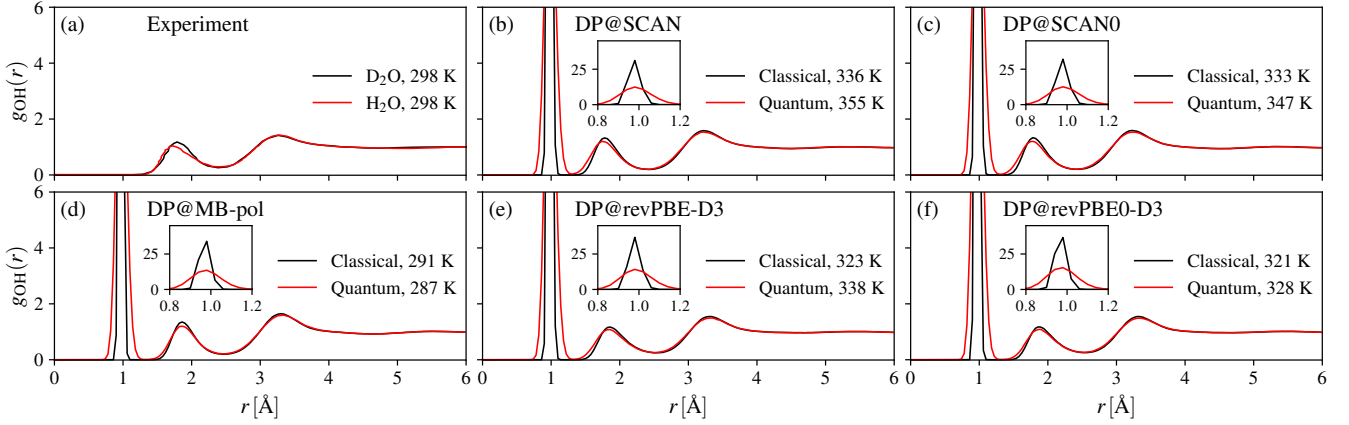


FIG. 14. O-H RDF  $g_{OH}(r)$  of liquid water. (a) Experimental result from [66]. (b)  $g_{OH}(r)$  of classical and quantum water calculated by the models at their predicted  $T_m^{cl} + 25$  K and  $T_m + 25$  K, respectively. The experimental result does not report the first peak of  $g_{OH}(r)$ , which corresponds to the intramolecular O-H interactions.

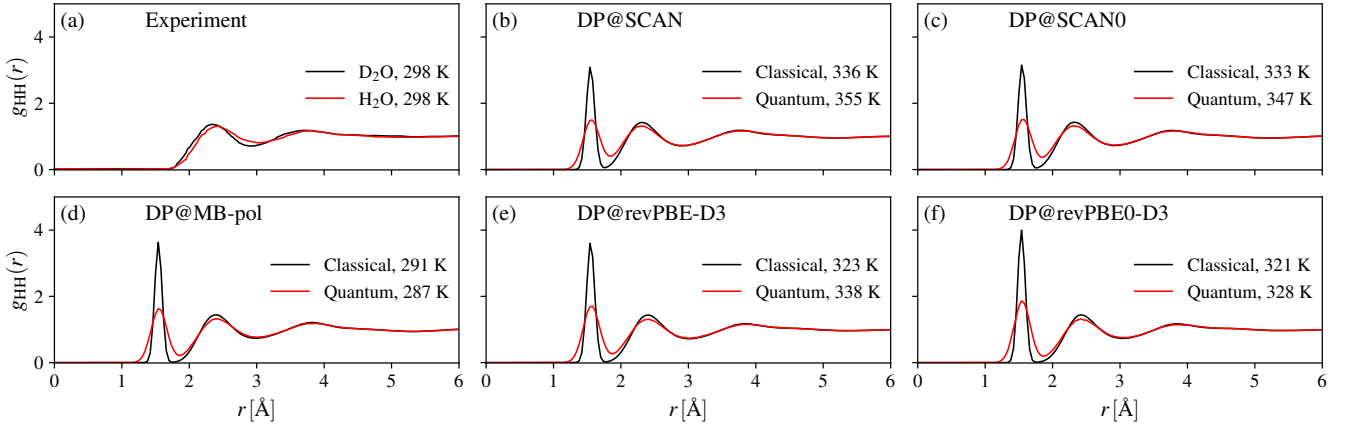


FIG. 15. H-H RDF  $g_{HH}(r)$  of liquid water. (a) Experimental result from [66]. (b)  $g_{HH}(r)$  of classical and quantum water calculated by the models at their predicted  $T_m^{cl} + 25$  K and  $T_m + 25$  K, respectively. The experimental result does not report the first peak of  $g_{HH}(r)$ , which corresponds to the intramolecular H-H interactions.

is broadened while the second peak remains unchanged, con-

sistent with the experimental effect. All models do not show

the softening at the first interstitial region in the experimental  $g_{OO}(r)$  and underestimate the lowering of the first peak. Moreover, the four DFT-based models show that NQEs slightly move the distribution to the left at  $2.4 \text{ \AA} < r < 2.7 \text{ \AA}$ , which does not appear in experiment. This implies that the strength of hydrogen bonds is slightly overestimated by these DFT-based models. In addition, although the experimental  $g_{OH}(r)$  and  $g_{HH}(r)$  do not report the first peaks, which correspond to the intramolecular interactions, the models predict  $g_{OH}(r)$  and  $g_{HH}(r)$  consistent with experiment.

In summary, the RDFs of water calculated at the corresponding effective room temperature of each model show good agreement with experiment. The consistency between calculated RDFs as well as their NQEs and experimental observations supports the accuracy of the calculated melting temperatures. The discrepancies between the predicted RDFs and the experimental  $g_{OO}(r)$  shown in FIG. ?? of the Letter also offer physical insights into the underlying DFT functionals on which the models are based.

#### IV. COMPARISON WITH PREVIOUS WORK

revPBE0-D3 is a widely used functional in the study of water, and various MLPs for water have been trained using this functional [13, 14, 28, 30, 31]. However, these MLPs report mutually inconsistent results:  $T_m$  higher than experiment [30], lower than experiment [31], or close to experiment [13, 14];  $\Delta\rho_{\text{liq-ice}}$  greater than experiment [31] or smaller than experiment [13, 30]; and  $T_{dm}$  above experiment [13, 30] or below experiment [31]. Since a MLP serves only as a surrogate for its underlying electronic structure method, different MLPs trained on the same functional should, in principle, yield consistent predictions. To clarify the source of these discrepancies, we compare our DP@revPBE0-D3 with two previously published models: the BPNN@revPBE0-D3 from Ref. [13], with a training protocol analogous to that of Ref. [14], and the NEP@revPBE0-D3 from Ref. [30]. These two MLPs were trained using similar revPBE0-D3 settings in CP2K, which we also adopted in our work, thus enabling a meaningful comparison based on a consistent underlying electronic structure method.

##### A. The BPNN Model for revPBE0-D3 DFT

Our findings on the revPBE0-D3-based MLP are different from those of Ref. [13], which used a BPNN model (hereafter called BPNN1) and a different training set. We show that our DP model is in better agreement with the revPBE0-D3 DFT. The O-O RDF  $g_{OO}(r)$  of classical water from AIMD is shown in FIG. ?? of the Letter, revealing a slightly overstructured profile compared to experiment. Our DP model closely reproduces the AIMD  $g_{OO}(r)$ , whereas the  $g_{OO}(r)$  reported in Ref. [13] shows more radial density in the interstitial region between the first two coordination shells.

To ensure that the observed differences do not originate from the network architecture, we construct a BPNN model

(hereafter referred to as BPNN2) using the same dataset employed to train the DP model. The dataset for DP and BPNN2 is generated with the same revPBE0-D3 DFT settings used for BPNN1, except for the MGRID CUTOFF: the DFT calculations for BPNN1 use a cutoff of 400 Ry, whereas those for BPNN2 and DP use the more converged value of 800 Ry as recommended in Ref. [43]. Nevertheless, increasing the cutoff is not expected to substantially affect the revPBE0-D3 DFT results.

To assess the accuracy of the three MLPs independently of their training sets, we extract 50 configurations of liquid water and 50 configurations of ice, together with their energies and forces, from the AIMD simulations reported in Subsection III A. We run AIMD simulations using cutoff values of 400 Ry and 800 Ry to construct test sets appropriate for evaluating BPNN1 and BPNN2 (and DP), respectively. As reported in FIG. 16, BPNN2 and DP make similarly accurate predictions on the test set, whereas BPNN1 displays a systematic energy bias of about 1.4 meV/atom for water and force errors that are nearly twice as large as those of BPNN2 and DP, as evidenced by the error distributions and root-mean-squared error (RMSE) values. The large test errors may explain the deviation of BPNN1 from AIMD results. The comparison among the three MLPs indicates that the issue of BPNN1 is due to the training dataset rather than the network architecture.

We now analyze the training dataset used for BPNN1 (hereafter called SET1) and the training dataset for both DP and BPNN2 (called SET2). We report in FIG. 17 the energy distributions of SET1 and SET2, respectively. The configurations of classical water in SET2 are sampled by MD simulations at around 300 K and their energy ranges are indicated by the red rectangle. In contrast, SET1 contains only a few configurations in this region and predominantly includes configurations corresponding to higher temperatures. Furthermore, SET2 includes configurations of both liquid water and ice sampled from classical MD and PIMD, while SET1 only includes configurations of liquid water. These two issues of SET1 lead to its large test error reported in FIG. 16 and thus its deviation from the AIMD simulations.

We now discuss the difference in  $T_m - T_m^{\text{cl}}$  reported in Ref. [13] with BPNN1 and in our work with DP. We use BPNN1, BPNN2, and DP models trained on revPBE0-D3 DFT to run an MTI calculation at 290 K and 1 bar. As given in FIG. 8, an MTI with fully converged number of beads results in  $\Delta\mu_{\text{ice-} \text{liq}}^{\text{qu}}(290 \text{ K}) - \Delta\mu_{\text{ice-} \text{liq}}^{\text{cl}}(290 \text{ K}) = -1.76(1)$  meV / H<sub>2</sub>O which increases the  $T_m$  of ice for 7 K. Here we use the number of beads 8, 16, 32, 32, 32 for  $y = 0.1, 0.2, 0.3, 0.4, 0.6, 1.0$ , and run each PIMD simulation for 100 ps. Other computational settings are the same as those used in Subsection II F. We report the  $\Delta g_{\text{ice-} \text{liq}}(y)$  values from these three models in FIG. 18. By integrating  $\Delta g_{\text{ice-} \text{liq}}(y)$  on  $y \in (0, 1)$  with the trapezoidal formula, we obtain  $\Delta\mu_{\text{ice-} \text{liq}}^{\text{qu}}(290 \text{ K}) - \Delta\mu_{\text{ice-} \text{liq}}^{\text{cl}}(290 \text{ K})$  and  $T_m - T_m^{\text{cl}}$  in TABLE VII. We find that BPNN1 predicts  $T_m - T_m^{\text{cl}} = -4$  K, in qualitative agreement with the result in Ref. [13]. In contrast, BPNN2 gives  $T_m - T_m^{\text{cl}} = +6$  K, very similar to the result of DP. These results emphasize the importance of a comprehensive dataset to capture subtle properties such as NQEs on

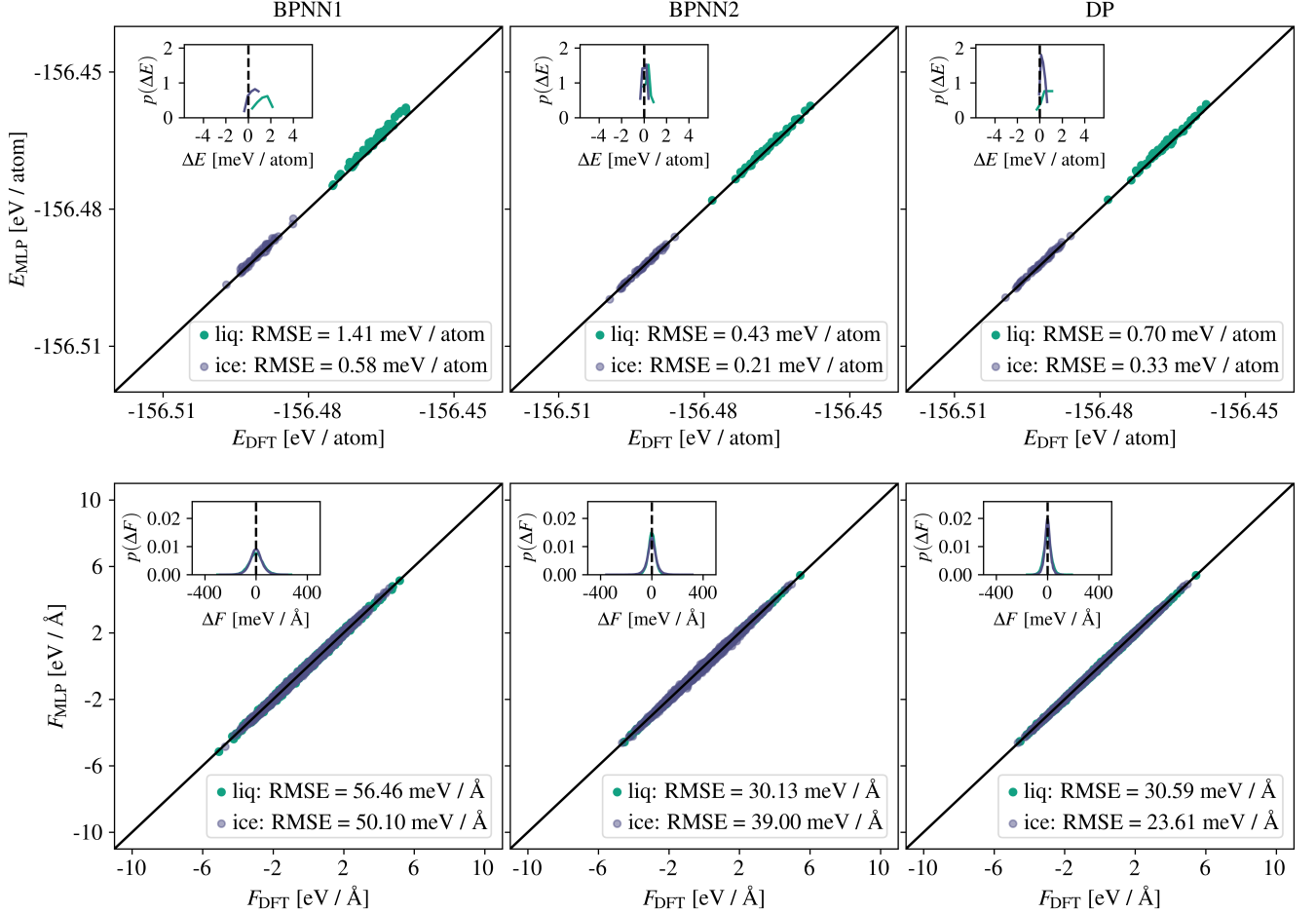


FIG. 16. Test errors of the three revPBE0-D3-based MLPs on test sets generated by AIMD simulations of liquid water and ice in the  $NpT$  ensemble at 300 K and 1 bar. The insets show the probability density distributions of the test errors of energy ( $\Delta E = E_{\text{MLP}} - E_{\text{DFT}}$ ) and force ( $\Delta F = F_{\text{MLP}} - F_{\text{DFT}}$ ). The test set include 50 configurations of water and 50 configurations of ice. BPNN1 is trained with SET1. BPNN2 and DP are trained with SET2. Compared to BPNN2 and DP, a systematic positive bias in the energy prediction for water and larger root-mean-squared errors (RMSEs) in the force prediction with BPNN1 are observed.

TABLE VII.  $\Delta\mu_{\text{ice}-\text{liq}}^{\text{qu}}(290 \text{ K}) - \Delta\mu_{\text{ice}-\text{liq}}^{\text{cl}}(290 \text{ K})$  from the MTI method calculated with three MLPs based on revPBE0-D3<sup>a</sup>

Model	Number of Beads	$\Delta\mu_{\text{ice}-\text{liq}}^{\text{qu}} - \Delta\mu_{\text{ice}-\text{liq}}^{\text{cl}}$	$T_m - T_m^{\text{cl}}$
DP <sup>b</sup>	8,16,32,64,64,64	-1.76 meV / H <sub>2</sub> O	+7 K
BPNN1	8,16,32,32,32,32	+0.82 meV / H <sub>2</sub> O	~ -4 K
BPNN2	8,16,32,32,32,32	-1.62 meV / H <sub>2</sub> O	~ +6 K
DP	8,16,32,32,32,32	-1.76 meV / H <sub>2</sub> O	~ +7 K

<sup>a</sup> We only perform MTI at 290 K and estimate the change in melting temperature approximately.

<sup>c</sup> The result in this line is reported in Subsection III D.

the melting temperature of ice.

## B. The NEP Model for revPBE0-D3 DFT

We also address the discrepancy between our results and those reported in Ref. [30]. Using a neuroevolution-potential

(NEP) [23] model trained on revPBE0-D3 DFT, Ref. [30] reports a density of 1.001 g/cm<sup>3</sup> for classical water at 298.15 K and 1 bar, which differs markedly from the value of 0.925 g/cm<sup>3</sup> obtained from our AIMD simulations at 300 K. In other words, the NEP model in Ref. [30] does not reproduce the underestimated densities of water and ice predicted by revPBE0-D3 in our work.

The NEP potential employs the same revPBE0-D3 settings as those used in Ref. [13], and therefore should, in principle, yield predictions for the properties of water that are consistent with our results. We attribute the observed inconsistency to the training dataset used for the NEP potential. This dataset was originally constructed for simulations in the  $NVT$  ensemble in Ref. [28] and would need to be extended appropriately in order to perform reliable  $NpT$  simulations.

In FIG. 19, we report the test errors of the NEP model from Ref. [30] on a test set consisting of 50 water configurations and 50 ice configurations. These configurations are extracted from  $NpT$  AIMD simulations of 64 H<sub>2</sub>O molecules at 300 K and 1

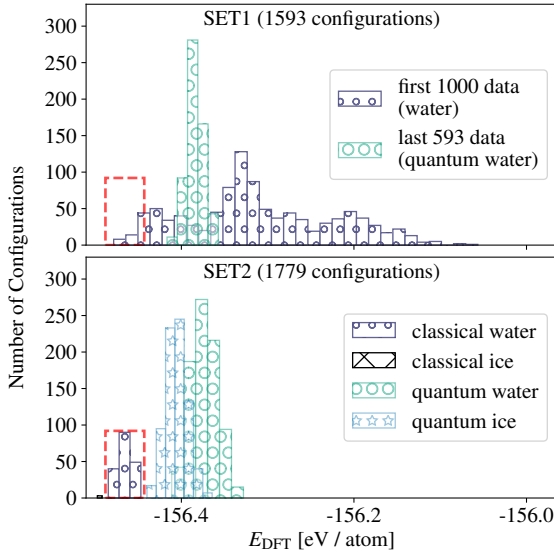


FIG. 17. Energy distributions of SET1 (for BPNN1) and SET2 (for BPNN2 and DP). The red rectangles highlight the energy ranges for liquid water configurations sampled with classical MD at around 300 K. SET1 has few configurations in this region.

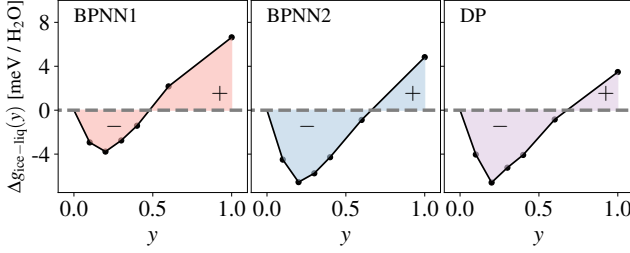


FIG. 18.  $\Delta g_{\text{ice-liq}}(y)$  calculated by BPNN1, BPNN2, and DP at 290 K and 1 bar. The "+" region is larger than the "-" region for BPNN1, resulting in  $T_m < T_m^{\text{cl}}$ ; for BPNN2 and DP the "+" region is smaller than "-", yielding  $T_m > T_m^{\text{cl}}$ .

bar, using an MGRID CUTOFF of 400 Ry. Similar to BPNN1, this NEP model exhibits a systematic energy bias of about 1.8 meV per atom for water and 1.0 meV per atom for ice, along with larger force errors compared to BPNN2 and DP. These results indicate that the NEP training dataset is insufficient for constructing a model intended for accurate *NpT* simulations at 300 K and 1 bar.

## V. CONCLUSIONS

By training MLPs trained on DFT and MB-pol and performing MD calculations including NQE, we provide a clear assessment of the capabilities of these MLPs in describing important properties of water related to the melting of ice. The MLP based on MB-pol makes qualitatively correct predictions on all properties considered. All DFT-based models incorrectly predict that NQE lower the melting point ( $T_m$ )

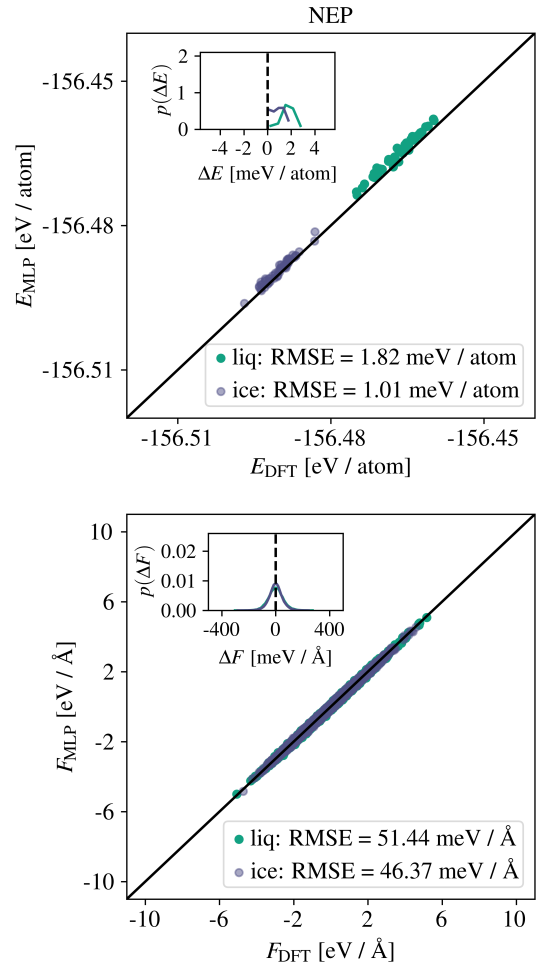


FIG. 19. Test error of the revPBE0-D3-based NEP model on a test set generated by AIMD simulations of liquid water and ice in the *NpT* ensemble at 300 K and 1 bar. The inset shows the probability density distributions of the test errors of energy ( $\Delta E = E_{\text{MLP}} - E_{\text{DFT}}$ ) and force ( $\Delta F = F_{\text{MLP}} - F_{\text{DFT}}$ ). The test set include 50 configurations of water and 50 configurations of ice.

of ice. For the temperature of density maximum ( $T_{\text{dm}}$ ) of liquid water, the DP@SCAN and DP@SCAN0 correctly predicts  $T_{\text{dm}} > T_m$ , while DP@revPBE-D3 and DP@revPBE0-D3 predict the opposite. For  $\Delta \rho_{\text{liq-ice}}$ , DP@SCAN and DP@SCAN0 make predictions close to experimental results, while DP@revPBE-D3 and DP@revPBE0-D3 significantly underestimate the value.

As discussed in the Letter, computing the RDFs of water at the effective “room temperature” predicted by the models yields results that are reasonably close to experiment. This suggests that evaluating room-temperature properties at each model’s predicted  $T_m + 25$  K is more appropriate than using the absolute temperature of 300 K. The remaining discrepancies between the predicted RDFs and experiment offer valuable insight into the limitations of current DFT functionals in capturing the strength of hydrogen bonding.

By comparing several MLPs for the same first-principles

method, we have emphasized the importance of building good datasets when training MLPs. MLP models are proxies for the underlying quantum mechanical models and extreme care should be taken when using these models for the prediction of a property as delicate as the sign of the isotope effect on the melting temperature of ice. The active learning procedure should thoroughly cover the phases and thermodynamic conditions under consideration to build a complete dataset for building reliable MLPs.

Our work presents strengths and limitations of different first-principles-based MLPs in modeling water, offering valuable references and insights for the computational study of aqueous systems in greater details.

## ACKNOWLEDGMENTS

We thank Ruiqi Gao, Han Wang, Jinzhe Zeng, and Linfeng Zhang for useful discussions. This work is supported by the Computational Chemical Sciences Center “Chemistry in So-

lution and at Interfaces” under Award No. DE-SC0019394 from the U.S. Department of Energy. We acknowledge the computational resources provided by the National Energy Research Scientific Computing Center (NERSC), which is supported by the U.S. Department of Energy (DOE), Office of Science under Contract No. DE-AC0205CH11231 and Princeton Research Computing at Princeton University. P.M.P. acknowledges funding from the Marie Skłodowska-Curie Cofund Programme of the European Commission project H2020-MSCA- COFUND-2020-101034228-WOLFRAM2. The models, data and input files supporting the calculations can be found at our GitHub repository [55].

## Appendix A: Derivation of Mass Thermodynamic Integration for the Quantum Correction to Chemical Potential

Here we derive Eq.(5). The partition function of the classical system with  $N$  atoms of masses  $m = (m_1, m_2, \dots, m_N)$  multiplied by a scaling factor  $\lambda$  is

$$Q^{\text{cl}}(\lambda) = \int \prod_{i=1}^N d\mathbf{p}_i d\mathbf{r}_i \exp \left\{ -\frac{1}{k_B T} \left[ \sum_{i=1}^N \frac{\mathbf{p}_i^2}{2\lambda m_i} + U(\mathbf{r}_1, \mathbf{r}_2, \dots, \mathbf{r}_N) \right] \right\}. \quad (\text{A1})$$

The partition function of the classical system with physical

masses is  $Q^{\text{cl}}(1)$ . Similarly, the partition function of a quantum system mapped to  $n$  beads is

$$Q_n^{\text{qu}}(\lambda) = \int \prod_{k=1}^n \prod_{i=1}^N d\mathbf{p}_i^{(k)} d\mathbf{r}_i^{(k)} \exp \left\{ -\frac{1}{k_B T} \sum_{k=1}^n \left[ \sum_{i=1}^N \frac{\mathbf{p}_i^{(k)2}}{2\lambda m_i} + \frac{1}{2} \lambda m_i \omega_n^2 (\mathbf{r}_i^{(k)} - \mathbf{r}_i^{(k+1)})^2 + \frac{1}{n} U(\mathbf{r}_1^{(k)}, \mathbf{r}_2^{(k)}, \dots, \mathbf{r}_N^{(k)}) \right] \right\} \quad (\text{A2})$$

with the condition  $\mathbf{r}_i^1 = \mathbf{r}_i^{n+1}$ , where  $\omega_n = \frac{\sqrt{n} k_B T}{\hbar}$ . We note that  $Q^{\text{cl}}(\infty) = Q_n^{\text{qu}}(\infty) = \int \prod_{i=1}^N d\mathbf{r}_i \exp \left[ -\frac{1}{k_B T} U(\mathbf{r}_1, \mathbf{r}_2, \dots, \mathbf{r}_N) \right]$  is equal to the configurational partition function of the classical system.

That is,  $Q^{\text{cl}}(\lambda) = Q^{\text{cl}}(\infty) \prod_{i=1}^N \left( \frac{2\pi\lambda m_i}{k_B T} \right)^{\frac{3}{2}}$ . For a system of  $N_{\text{H}_2\text{O}}$  molecules in phase  $\alpha$ , the quantum correction to the chemical potential is

$$\begin{aligned} \Delta\mu_{\alpha}^{\text{qu}-\text{cl}}(T) &= \mu_{\alpha}(T) - \mu_{\alpha}^{\text{cl}}(T) = -\frac{k_B T}{N_{\text{H}_2\text{O}}} \ln \frac{Q_n^{\text{qu}}(1)}{Q^{\text{cl}}(1)} = -\frac{k_B T}{N_{\text{H}_2\text{O}}} \ln \frac{Q_n^{\text{qu}}(1)}{Q_n^{\text{qu}}(\infty)} + \frac{k_B T}{N_{\text{H}_2\text{O}}} \ln \frac{Q^{\text{cl}}(\infty)}{Q^{\text{cl}}(1)} \\ &= \frac{k_B T}{N_{\text{H}_2\text{O}}} \int_1^{\infty} \frac{d}{d\lambda} \ln Q_n^{\text{qu}}(\lambda) d\lambda - \frac{k_B T}{N_{\text{H}_2\text{O}}} \int_1^{\infty} \frac{d}{d\lambda} \ln \frac{Q^{\text{cl}}(\infty)}{Q^{\text{cl}}(\lambda)} d\lambda. \end{aligned} \quad (\text{A3})$$

The integrand of the first term in Eq. (A3) is

$$\begin{aligned} \frac{d}{d\lambda} \ln Q_n^{\text{qu}}(\lambda) &= \frac{1}{Q_n^{\text{qu}}(\lambda)} \frac{d}{d\lambda} Q_n^{\text{qu}}(\lambda) = \frac{1}{\lambda k_B T} \left\langle \sum_{k=1}^n \sum_{i=1}^N \left[ \frac{\mathbf{p}_i^{(k)}{}^2}{2\lambda m_i} - \frac{1}{2} \lambda m_i \omega_n^2 \left( \mathbf{r}_i^{(k)} - \mathbf{r}_i^{(k+1)} \right)^2 \right] \right\rangle_{\lambda} \\ &= \frac{1}{\lambda k_B T} \left\langle \frac{3nN}{2} k_B T - \sum_{k=1}^n \sum_{i=1}^N \frac{1}{2} \lambda m_i \omega_n^2 \left( \mathbf{r}_i^{(k)} - \mathbf{r}_i^{(k+1)} \right)^2 \right\rangle_{\lambda} \end{aligned} \quad (\text{A4})$$

where  $\langle \cdot \rangle_{\lambda}$  is the ensemble average associated with the partition function  $Q_n^{\text{qu}}(\lambda)$ . The quantity in  $\langle \cdot \rangle_{\lambda}$  of Eq. (A4) is the primitive quantum kinetic energy estimator  $K_{\text{PR},\alpha}(\frac{\lambda m}{\hbar^2})$ , which is equivalent to the centroid-virial estimator  $K_{\text{CV},\alpha}(\frac{\lambda m}{\hbar^2})$  as defined in Eq. (7), multiplied by  $N_{\text{H}_2\text{O}}$ . Thus the first term in Eq. (A3) is equal to  $\int_1^{\infty} \langle K_{\text{CV},\alpha}(\frac{\lambda m}{\hbar^2}) \rangle \frac{d\lambda}{\lambda}$ . Using change of variable  $\lambda = 1/y^2$  this term becomes

$$2 \int_0^1 \left\langle K_{\text{CV},\alpha} \left( \frac{m}{y^2 \hbar^2} \right) \right\rangle \frac{dy}{y}. \quad (\text{A5})$$

The integrand of the second term in Eq. (A3) is

$$\frac{d}{d\lambda} \ln \frac{Q^{\text{cl}}(\infty)}{Q^{\text{cl}}(\lambda)} = \frac{d}{d\lambda} \frac{3}{2} \sum_{i=1}^N \ln \left( \frac{2\pi\lambda m_i}{k_B T} \right) = \frac{3N}{2\lambda}. \quad (\text{A6})$$

Then the second term in Eq. (A3) is equal to  $-\int_1^{\infty} \frac{3Nk_B T}{2N_{\text{H}_2\text{O}}} \frac{d\lambda}{\lambda}$ , or equivalently,

$$-2 \int_0^1 \frac{3Nk_B T}{2N_{\text{H}_2\text{O}}} \frac{dy}{y}. \quad (\text{A7})$$

Combining the two terms in Eqs. (A5) and (A7) gives Eqs. (5) and (6).

## Appendix B: Derivation of the Lowest-order Expansion of $g_{\alpha}(y)$

We derive Eq. (10) starting from the Wigner-Kirkwood (WK) expansion [61]. The WK expansion gives the leading quantum correction to the classical partition function of phase

$\alpha$  as an expansion in even powers of  $\hbar$ ,

$$Q_{\alpha}^{\text{qu}} = Q_{\alpha}^{\text{cl}} \left[ 1 + \frac{\beta^2 \hbar^2}{24} \sum_i \frac{1}{m_i} \langle \|\nabla_i U\|^2 \rangle_{\alpha}^{\text{cl}} + \mathcal{O}(\hbar^4) \right], \quad (\text{B1})$$

where  $\langle \cdot \rangle_{\alpha}^{\text{cl}}$  denotes a classical  $NpT$  ensemble average.

The quantum correction to the chemical potential is

$$\Delta\mu_{\alpha}^{\text{qu}-\text{cl}}(T) = -\frac{k_B T}{N_{\text{H}_2\text{O}}} \ln \left( \frac{Q_{\alpha}^{\text{qu}}}{Q_{\alpha}^{\text{cl}}} \right). \quad (\text{B2})$$

Using  $\ln(1+x) = x + \mathcal{O}(x^2)$ , we obtain

$$\Delta\mu_{\alpha}^{\text{qu}-\text{cl}}(T) = -\frac{k_B T}{N_{\text{H}_2\text{O}}} \left[ \frac{\beta^2 \hbar^2}{24} \sum_i \frac{1}{m_i} \langle \|\nabla_i U\|^2 \rangle_{\alpha}^{\text{cl}} \right] + \mathcal{O}(\hbar^4). \quad (\text{B3})$$

Using  $\beta = \frac{1}{k_B T}$  and  $\nabla_i U = -\mathbf{F}_i$ , this becomes

$$\Delta\mu_{\alpha}^{\text{qu}-\text{cl}}(T) = \frac{\hbar^2}{24k_B T N_{\text{H}_2\text{O}}} \sum_i \frac{1}{m_i} \langle \|\mathbf{F}_i\|^2 \rangle_{\alpha}^{\text{cl}} + \mathcal{O}(\hbar^4). \quad (\text{B4})$$

In mass thermodynamic integration we introduce the variable  $y$  (with  $y \in [0, 1]$ ) such that scaling the nuclear masses as  $m_i \rightarrow m_i/y^2$  is equivalent to scaling the Planck constant as  $\hbar \rightarrow y\hbar$ . Therefore, Eq. (B4) implies the small- $y$  expansion

$$\Delta\mu_{\alpha}^{\text{qu}-\text{cl}}(T; y) = \frac{(y\hbar)^2}{24k_B T N_{\text{H}_2\text{O}}} \sum_i \frac{1}{m_i} \langle \|\mathbf{F}_i\|^2 \rangle_{\alpha}^{\text{cl}} + \mathcal{O}(y^4). \quad (\text{B5})$$

Since  $g_{\alpha}(y) = d\Delta\mu_{\alpha}^{\text{qu}-\text{cl}}(T; y)/dy$ , we obtain

$$g_{\alpha}(y) = \frac{y\hbar^2}{12T N_{\text{H}_2\text{O}}} \sum_i \frac{1}{m_i} \langle \|\mathbf{F}_i\|^2 \rangle_{\alpha}^{\text{cl}} + \mathcal{O}(y^3), \quad (\text{B6})$$

and hence

$$g_{\alpha} \bigg|_{y=0} = \frac{\hbar^2}{12T^2 N_{\text{H}_2\text{O}}} \sum_i \frac{1}{m_i} \langle \|\mathbf{F}_i\|^2 \rangle_{\alpha}^{\text{cl}}, \quad (\text{B7})$$

which is Eq. (10).

---

[1] P. Gallo, K. Amann-Winkel, C. A. Angell, M. A. Anisimov, F. Caupin, C. Chakravarty, E. Laskaris, T. Loerting, A. Z. Panagiotopoulos, J. Russo, J. A. Sellberg, H. E. Stanley, H. Tanaka, C. Vega, L. Xu, and L. G. M. Pettersson, Water: A Tale of Two Liquids, Chem. Rev. **116**, 7463 (2016).  
[2] L. Ruiz Pestana, O. Marsalek, T. E. Markland, and T. Head-Gordon, The Quest for Accurate Liquid Water Properties from First Principles, J. Phys. Chem. Lett. **9**, 5009 (2018).

[3] J. Sun, A. Ruzsinszky, and J. Perdew, Strongly Constrained and Appropriately Normed Semilocal Density Functional, *Phys. Rev. Lett.* **115**, 036402 (2015).

[4] V. Babin, C. Leforestier, and F. Paesani, Development of a “First Principles” Water Potential with Flexible Monomers: Dimer Potential Energy Surface, VRT Spectrum, and Second Virial Coefficient, *J. Chem. Theory Comput.* **9**, 5395 (2013).

[5] V. Babin, G. R. Medders, and F. Paesani, Development of a “First Principles” Water Potential with Flexible Monomers. II: Trimer Potential Energy Surface, Third Virial Coefficient, and Small Clusters, *J. Chem. Theory Comput.* **10**, 1599 (2014).

[6] G. R. Medders, V. Babin, and F. Paesani, Development of a “First-Principles” Water Potential with Flexible Monomers. III. Liquid Phase Properties, *J. Chem. Theory Comput.* **10**, 2906 (2014).

[7] S. K. Reddy, S. C. Straight, P. Bajaj, C. Huy Pham, M. Riera, D. R. Moberg, M. A. Morales, C. Knight, A. W. Götz, and F. Paesani, On the accuracy of the MB-pol many-body potential for water: Interaction energies, vibrational frequencies, and classical thermodynamic and dynamical properties from clusters to liquid water and ice, *The Journal of Chemical Physics* **145**, 194504 (2016).

[8] F. Paesani, Getting the Right Answers for the Right Reasons: Toward Predictive Molecular Simulations of Water with Many-Body Potential Energy Functions, *Acc. Chem. Res.* **49**, 1844 (2016).

[9] M. Chen, H.-Y. Ko, R. C. Remsing, M. F. Calegari Andrade, B. Santra, Z. Sun, A. Selloni, R. Car, M. L. Klein, J. P. Perdew, and X. Wu, Ab initio theory and modeling of water, *Proceedings of the National Academy of Sciences* **114**, 10846 (2017).

[10] O. Marsalek and T. E. Markland, Quantum Dynamics and Spectroscopy of Ab Initio Liquid Water: The Interplay of Nuclear and Electronic Quantum Effects, *J. Phys. Chem. Lett.* **8**, 1545 (2017).

[11] F. Tang, Z. Li, C. Zhang, S. G. Louie, R. Car, D. Y. Qiu, and X. Wu, Many-body effects in the X-ray absorption spectra of liquid water, *Proceedings of the National Academy of Sciences* **119**, e2201258119 (2022).

[12] P. M. Piaggi, A. Z. Panagiotopoulos, P. G. Debenedetti, and R. Car, Phase Equilibrium of Water with Hexagonal and Cubic Ice Using the SCAN Functional, *J. Chem. Theory Comput.* **17**, 3065 (2021).

[13] B. Cheng, E. A. Engel, J. Behler, C. Dellago, and M. Ceriotti, Ab initio thermodynamics of liquid and solid water, *Proceedings of the National Academy of Sciences* **116**, 1110 (2019).

[14] A. Reinhardt and B. Cheng, Quantum-mechanical exploration of the phase diagram of water, *Nat Commun* **12**, 588 (2021).

[15] L. Zhang, H. Wang, R. Car, and W. E, Phase Diagram of a Deep Potential Water Model, *Phys. Rev. Lett.* **126**, 236001 (2021).

[16] F. Sciortino, Y. Zhai, S. L. Bore, and F. Paesani, Constraints on the location of the liquid–liquid critical point in water, *Nat. Phys.* **21**, 480 (2025).

[17] M. Calegari Andrade, R. Car, and A. Selloni, Probing the self-ionization of liquid water with ab initio deep potential molecular dynamics, *Proceedings of the National Academy of Sciences* **120**, e2302468120 (2023).

[18] P. M. Piaggi, J. Weis, A. Z. Panagiotopoulos, P. G. Debenedetti, and R. Car, Homogeneous ice nucleation in an ab initio machine learning model of water, *arXiv:2203.01376 [cond-mat, physics:physics]* (2022).

[19] L. Zhang, J. Han, H. Wang, R. Car, and W. E, Deep Potential Molecular Dynamics: A Scalable Model with the Accuracy of Quantum Mechanics, *Phys. Rev. Lett.* **120**, 143001 (2018).

[20] H. Wang, L. Zhang, J. Han, and W. E, DeePMD-kit: A deep learning package for many-body potential energy representation and molecular dynamics, *Computer Physics Communications* **228**, 178 (2018).

[21] J. Zeng, D. Zhang, D. Lu, P. Mo, Z. Li, Y. Chen, M. Rynik, L. Huang, Z. Li, S. Shi, Y. Wang, H. Ye, P. Tu, J. Yang, Y. Ding, Y. Li, D. Tisi, Q. Zeng, H. Bao, Y. Xia, J. Huang, K. Muraoka, Y. Wang, J. Chang, F. Yuan, S. L. Bore, C. Cai, Y. Lin, B. Wang, J. Xu, J.-X. Zhu, C. Luo, Y. Zhang, R. E. A. Goodall, W. Liang, A. K. Singh, S. Yao, J. Zhang, R. Wentzcovitch, J. Han, J. Liu, W. Jia, D. M. York, W. E, R. Car, L. Zhang, and H. Wang, DeePMD-kit v2: A software package for deep potential models, *The Journal of Chemical Physics* **159**, 054801 (2023).

[22] J. Behler and M. Parrinello, Generalized Neural-Network Representation of High-Dimensional Potential-Energy Surfaces, *Phys. Rev. Lett.* **98**, 146401 (2007).

[23] Z. Fan, Z. Zeng, C. Zhang, Y. Wang, K. Song, H. Dong, Y. Chen, and T. Ala-Nissila, Neuroevolution machine learning potentials: Combining high accuracy and low cost in atomistic simulations and application to heat transport, *Phys. Rev. B* **104**, 104309 (2021).

[24] Z. Fan, Y. Wang, P. Ying, K. Song, J. Wang, Y. Wang, Z. Zeng, K. Xu, E. Lindgren, J. M. Rahm, A. J. Gabourie, J. Liu, H. Dong, J. Wu, Y. Chen, Z. Zhong, J. Sun, P. Erhart, Y. Su, and T. Ala-Nissila, GPUMD: A package for constructing accurate machine-learned potentials and performing highly efficient atomistic simulations, *The Journal of Chemical Physics* **157**, 114801 (2022).

[25] M. Ceriotti, W. Fang, P. G. Kusalik, R. H. McKenzie, A. Michaelides, M. A. Morales, and T. E. Markland, Nuclear Quantum Effects in Water and Aqueous Systems: Experiment, Theory, and Current Challenges, *Chem. Rev.* **116**, 7529 (2016).

[26] M. Ceriotti, M. Parrinello, T. E. Markland, and D. E. Manolopoulos, Efficient stochastic thermostatting of path integral molecular dynamics, *The Journal of Chemical Physics* **133**, 124104 (2010).

[27] S. L. Bore and F. Paesani, Realistic phase diagram of water from “first principles” data-driven quantum simulations, *Nat Commun* **14**, 3349 (2023).

[28] C. Schran, K. Brezina, and O. Marsalek, Committee neural network potentials control generalization errors and enable active learning, *The Journal of Chemical Physics* **153**, 104105 (2020).

[29] K. Xu, T. Liang, N. Xu, P. Ying, S. Chen, N. Wei, J. Xu, and Z. Fan, NEP-MB-pol: a unified machine-learned framework for fast and accurate prediction of water’s thermodynamic and transport properties, *npj Comput Mater* **11**, 279 (2025).

[30] Z. Chen, M. L. Berrens, K.-T. Chan, Z. Fan, and D. Donadio, Thermodynamics of Water and Ice from a Fast and Scalable First-Principles Neuroevolution Potential, *J. Chem. Eng. Data* **69**, 128 (2024).

[31] P. Montero de Hijes, C. Dellago, R. Jinnouchi, and G. Kresse, Density isobar of water and melting temperature of ice: Assessing common density functionals, *The Journal of Chemical Physics* **161**, 131102 (2024).

[32] Y. Zhang and W. Yang, Comment on “Generalized Gradient Approximation Made Simple”, *Phys. Rev. Lett.* **80**, 890 (1998).

[33] S. Grimme, J. Antony, S. Ehrlich, and H. Krieg, A consistent and accurate *ab initio* parametrization of density functional dispersion correction (DFT-D) for the 94 elements H-Pu, *The Journal of Chemical Physics* **132**, 154104 (2010).

[34] C. Adamo and V. Barone, Toward reliable density functional methods without adjustable parameters: The PBE0 model, *The Journal of Chemical Physics* **110**, 6158 (1999).

[35] K. Hui and J.-D. Chai, SCAN-based hybrid and double-hybrid density functionals from models without fitted parameters, *The Journal of Chemical Physics* **144**, 044114 (2016).

[36] P. Giannozzi, S. Baroni, N. Bonini, M. Calandra, R. Car, C. Cavazzoni, D. Ceresoli, G. L. Chiarotti, M. Cococcioni, I. Dabo, A. Dal Corso, S. De Gironcoli, S. Fabris, G. Fratesi, R. Gebauer, U. Gerstmann, C. Gougoussis, A. Kokalj, M. Lazzeri, L. Martin-Samos, N. Marzari, F. Mauri, R. Mazzarello, S. Paolini, A. Pasquarello, L. Paulatto, C. Sbraccia, S. Scandolo, G. Sclauzero, A. P. Seitsonen, A. Smogunov, P. Umari, and R. M. Wentzcovitch, QUANTUM ESPRESSO: a modular and open-source software project for quantum simulations of materials, *J. Phys.: Condens. Matter* **21**, 395502 (2009).

[37] P. Giannozzi, O. Baseggio, P. Bonfà, D. Brunato, R. Car, I. Carnimeo, C. Cavazzoni, S. de Gironcoli, P. Delugas, F. Ferrari Ruffino, A. Ferretti, N. Marzari, I. Timrov, A. Urru, and S. Baroni, Quantum ESPRESSO toward the exascale, *The Journal of Chemical Physics* **152**, 154105 (2020).

[38] M. A. L. Marques, M. J. T. Oliveira, and T. Burnus, Libxc: A library of exchange and correlation functionals for density functional theory, *Computer Physics Communications* **183**, 2272 (2012).

[39] S. Lehtola, C. Steigemann, M. J. T. Oliveira, and M. A. L. Marques, Recent developments in libxc — A comprehensive library of functionals for density functional theory, *SoftwareX* **7**, 1 (2018).

[40] D. R. Hamann, Optimized norm-conserving Vanderbilt pseudopotentials, *Phys. Rev. B* **88**, 085117 (2013).

[41] J. Hutter, M. Iannuzzi, F. Schiffmann, and J. VandeVondele, cp2k: atomistic simulations of condensed matter systems, *WIREs Computational Molecular Science* **4**, 15 (2014).

[42] B. Cheng, <https://github.com/BingqingCheng/ice-in-water/blob/master/cp2k/ice.cp2k>.

[43] B. Monserrat, J. G. Brandenburg, E. A. Engel, and B. Cheng, Liquid water contains the building blocks of diverse ice phases, *Nat Commun* **11**, 5757 (2020).

[44] M. Guidon, J. Hutter, and J. VandeVondele, Auxiliary Density Matrix Methods for Hartree-Fock Exchange Calculations, *J. Chem. Theory Comput.* **6**, 2348 (2010).

[45] C. Zhang, F. Tang, M. Chen, J. Xu, L. Zhang, D. Y. Qiu, J. P. Perdew, M. L. Klein, and X. Wu, Modeling Liquid Water by Climbing up Jacob's Ladder in Density Functional Theory Facilitated by Using Deep Neural Network Potentials, *J. Phys. Chem. B* **125**, 11444 (2021).

[46] D. R. Hamann, M. Schlüter, and C. Chiang, Norm-Conserving Pseudopotentials, *Phys. Rev. Lett.* **43**, 1494 (1979).

[47] D. Vanderbilt, Optimally smooth norm-conserving pseudopotentials, *Phys. Rev. B* **32**, 8412 (1985).

[48] A. P. Gaiduk, F. Gygi, and G. Galli, Density and Compressibility of Liquid Water and Ice from First-Principles Simulations with Hybrid Functionals, *J. Phys. Chem. Lett.* **6**, 2902 (2015).

[49] J. Han, L. Zhang, R. Car, and W. E, Deep Potential: A General Representation of a Many-Body Potential Energy Surface, *CiCP* **23**, 10.4208/cicp.OA-2017-0213 (2018).

[50] L. Zhang, J. Han, H. Wang, W. Saidi, R. Car, and W. E, End-to-end Symmetry Preserving Inter-atomic Potential Energy Model for Finite and Extended Systems, in *Advances in Neural Information Processing Systems*, Vol. 31 (2018).

[51] L. Zhang, D.-Y. Lin, H. Wang, R. Car, and W. E, Active learning of uniformly accurate interatomic potentials for materials simulation, *Phys. Rev. Mater.* **3**, 023804 (2019).

[52] Y. Zhang, H. Wang, W. Chen, J. Zeng, L. Zhang, H. Wang, and W. E, DP-GEN: A concurrent learning platform for the generation of reliable deep learning based potential energy models, *Computer Physics Communications* **253**, 107206 (2020).

[53] S. Plimpton, Fast Parallel Algorithms for Short-Range Molecular Dynamics, *Journal of Computational Physics* **117**, 1 (1995).

[54] A. P. Thompson, H. M. Aktulga, R. Berger, D. S. Bolintineanu, W. M. Brown, P. S. Crozier, P. J. in 't Veld, A. Kohlmeyer, S. G. Moore, T. D. Nguyen, R. Shan, M. J. Stevens, J. Tranchida, C. Trott, and S. J. Plimpton, LAMMPS - a flexible simulation tool for particle-based materials modeling at the atomic, meso, and continuum scales, *Computer Physics Communications* **271**, 108171 (2022).

[55] Y. Li, <https://github.com/Yi-FanLi/NQE-Ice-Tm>.

[56] G. Bussi, T. Zykova-Timan, and M. Parrinello, Isothermal-isobaric molecular dynamics using stochastic velocity rescaling, *The Journal of Chemical Physics* **130**, 074101 (2009).

[57] <https://github.com/deepmodeling/dpti> (2024).

[58] S. Habershon, T. E. Markland, and D. E. Manolopoulos, Competing quantum effects in the dynamics of a flexible water model, *J. Chem. Phys.* **131**, 024501 (2009).

[59] M. Matsumoto, T. Yagasaki, and H. Tanaka, GenIce: Hydrogen-Disordered Ice Generator, *Journal of Computational Chemistry* **39**, 61 (2018).

[60] S. L. Bore and F. Paesani, *Quantum phase diagram of water*, preprint (Chemistry, 2023).

[61] E. Wigner, On the Quantum Correction For Thermodynamic Equilibrium, *Phys. Rev.* **40**, 749 (1932).

[62] G. E. Uhlenbeck and L. Gropper, The Equation of State of a Non-ideal Einstein-Bose or Fermi-Dirac Gas, *Phys. Rev.* **41**, 79 (1932).

[63] J. G. Kirkwood, Quantum Statistics of Almost Classical Assemblies, *Phys. Rev.* **44**, 31 (1933).

[64] L. Landau and E. Lifshitz, *Statistical Physics, Volume 5 of Course of Theoretical Physics*, second revised and enlarged ed. (Pergamon Press, 1969) pp. 98–104.

[65] P. M. Piaggi and R. Car, Phase equilibrium of liquid water and hexagonal ice from enhanced sampling molecular dynamics simulations, *The Journal of Chemical Physics* **152**, 204116 (2020).

[66] A. K. Soper and C. J. Benmore, Quantum Differences between Heavy and Light Water, *Phys. Rev. Lett.* **101**, 065502 (2008).

# Supplemental Material for Ab Initio Melting Properties of Water and Ice from Machine Learning Potentials Simulations

Yifan Li,<sup>1</sup> Bingjia Yang,<sup>1</sup> Chunyi Zhang,<sup>2</sup> Axel Gomez,<sup>1</sup> Pinchen Xie,<sup>3</sup> Yixiao Chen,<sup>3</sup> Pablo M. Piaggi,<sup>4,5</sup> and Roberto Car<sup>1,3,6,7</sup>

<sup>1</sup>*Department of Chemistry, Princeton University, Princeton, NJ 08544, USA*

<sup>2</sup>*Eastern Institute of Technology, Ningbo, Zhejiang 315200, China*

<sup>3</sup>*Program in Applied and Computational Mathematics, Princeton University, Princeton, NJ 08544, USA*

<sup>4</sup>*CIC nanoGUNE BRTA, Tolosa Hiribidea 76, 20018 Donostia-San Sebastián, Spain*

<sup>5</sup>*Ikerbasque, Basque Foundation for Science, 48013 Bilbao, Spain*

<sup>6</sup>*Department of Physics, Princeton University, Princeton, NJ 08544, USA*

<sup>7</sup>*Princeton Institute for the Science and Technology of Materials, Princeton University, Princeton, NJ 08544, USA*

## I. DEEP POTENTIAL MODELS

### A. Training Dataset

The overall number of training data of each DP model is summarized in Table S I.

TABLE S I. The Composition of Dataset of Each Model

Functional	Classical Water	Quantum Water	Classical Ice	Quantum Ice	Total
revPBE-D3	4142	720	385	686	5933
revPBE0-D3	179	749	3	847	1778
SCAN	1	3553	0	1153	4707
SCAN0	0	7749	0	96	7845

### B. Training Error

In FIG. S1 energies and forces predicted by the four DP models are compared with the corresponding DFT values for the configurations in the training dataset. The resulting mean absolute error (MAE) and root mean square error (RMSE) are reported in TABLE S II.

TABLE S II. The Training MAE and RMSE of Each Model

Model for Functional	Energy MAE [meV / atom]	Energy RMSE [meV / atom]	Force MAE [meV / Å]	Force RMSE [meV / Å]
revPBE-D3	0.289	0.372	27.3	36.0
revPBE0-D3	0.300	0.388	28.0	37.0
SCAN	0.475	0.599	67.5	97.5
SCAN0	0.667	0.825	52.5	71.6

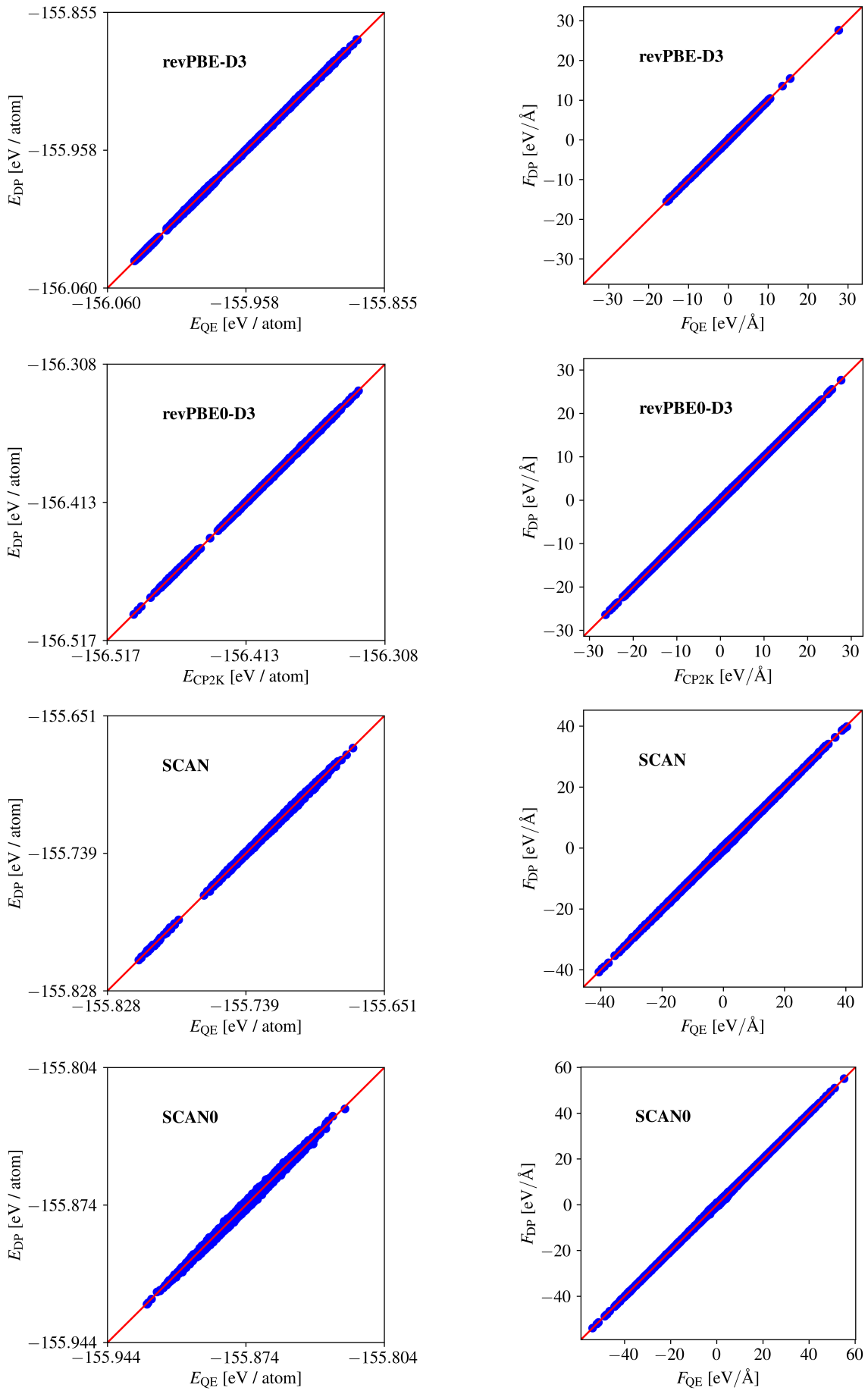


FIG. S1. DFT energies and forces compared with the values predicted by DP models.

## II. CLASSICAL THERMODYNAMIC INTEGRATION

The chemical potentials calculated in Step 3, Hamiltonian Thermodynamic Integration, are listed in TABLE S III.

TABLE S III. The Chemical Potential  $\mu$  of Water and Ice at 1 bar Calculated with HTI<sup>a</sup>

Model	Phase	$T_{\text{init}}$ [K]	$P$ [bar]	$\mu(P, T_{\text{init}})$ [eV / H <sub>2</sub> O]
DP@revPBE-D3	Ice Ih	150	1	-468.0095 (2)
DP@revPBE-D3	Ice Ih	300	1	-467.9641 (4)
DP@revPBE-D3	Water	300	1	-467.9641 (1)
DP@revPBE-D3	Water	350	1	-467.9817 (1)
DP@revPBE0-D3	Ice Ih	150	1	-469.3987 (2)
DP@revPBE0-D3	Ice Ih	300	1	-469.3517 (4)
DP@revPBE0-D3	Water	300	1	-469.3526 (2)
DP@revPBE0-D3	Water	350	1	-469.3701 (2)
DP@SCAN	Ice Ih	150	1	-467.3948 (2)
DP@SCAN	Ice Ih	300	1	-467.3439 (4)
DP@SCAN	Water	300	1	-467.3409 (2)
DP@SCAN	Water	350	1	-467.3535 (2)
DP@SCAN0	Ice Ih	150	1	-467.9174 (2)
DP@SCAN0	Ice Ih	300	1	-467.8666 (4)
DP@SCAN0	Water	300	1	-467.8636 (2)
DP@SCAN0	Water	350	1	-467.8764 (2)

<sup>a</sup> The value in parentheses is the statistical uncertainty in the last digit.

### III. MASS THERMODYNAMIC INTEGRATION AT DIFFERENT TEMPERATURES

We report the  $\Delta g_{\text{ice-liq}}(y)$  curves at different temperatures in FIG. S2.

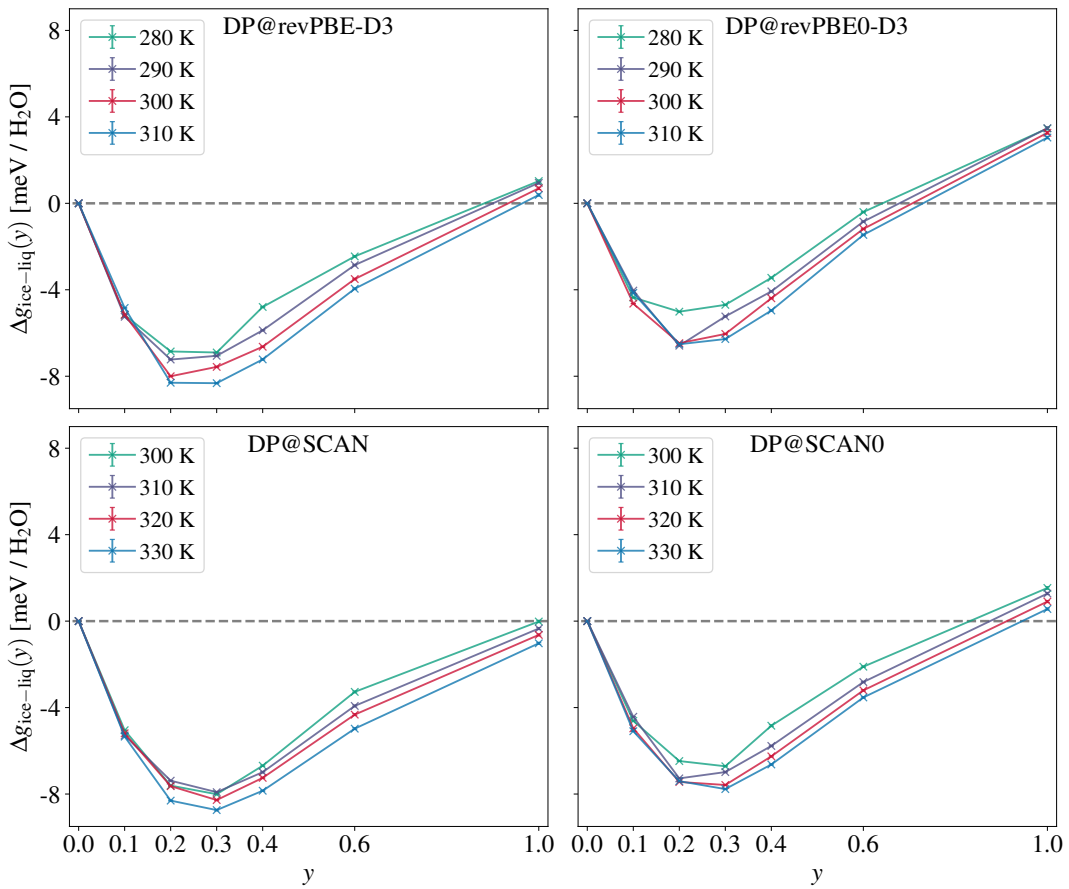
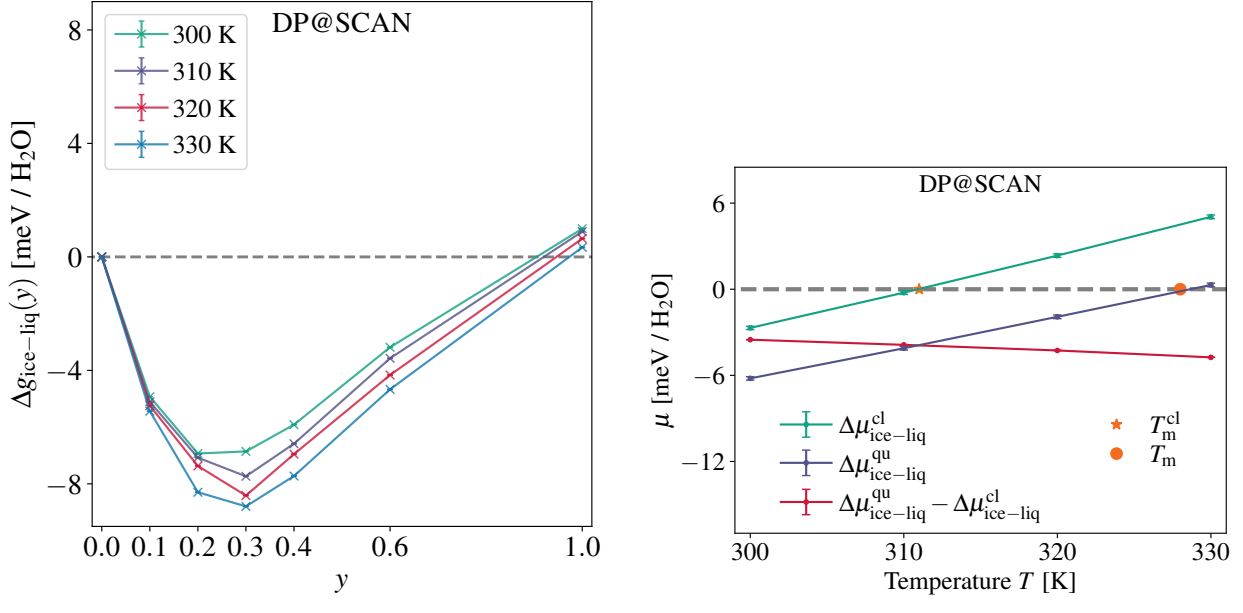


FIG. S2.  $\Delta g_{\text{ice-liq}}(y)$  curves for each functional at different temperatures around the melting point.

#### IV. MASS THERMODYNAMIC INTEGRATION WITH REDUCED NUMBER OF BEADS

We validate the  $T_m$  for DP@SCAN obtained with the direct coexistence method by performing the mass thermodynamic integration calculation with reduced number of beads, i.e., 8, 16, 32, 32, 32 for  $y = 0.1, 0.2, 0.3, 0.4, 0.6, 1.0$ , respectively.



(a)  $\Delta g_{\text{ice-liq}}(y)$  curves for SCAN with reduced number of beads at different temperatures around the melting point.

(b) The chemical potential differences obtained with reduced number of beads.

FIG. S3. The mass thermodynamic integration result for DP@SCAN with reduced number of beads. The chemical potential differences yield  $T_m = 328 \pm 1$  K, which is slightly lower than  $T_m = 330 \pm 1$  K obtained with fully converged numbers of beads, and agrees with  $T_m = 324 \pm 3$  K obtained in the direct coexistence simulations within error bar.